Modeling of surface-wave discharges with cylindrical symmetry

L. L. Alves*
Instituto de Plasmas e Fusão Nuclear, Instituto Superior Técnico, Av. Rovisco Pais, 1049-001 Lisboa, Portugal

S. Letout† and C. Boisse-Laporte
Laboratoire de Physique des Gaz et des Plasmas, Université Paris-Sud, 91405 Orsay Cedex, France
(Received 28 March 2008; published 8 January 2009)

This paper presents the modeling of microwave (2.45 GHz) discharges with cylindrical symmetry, produced in the absence of an external magnetic field by TM_{00} surface waves (SW) within either cylindrical or coaxial structures. A stationary, one-dimensional (radial) moment model (including the continuity and the momentum-transfer equations for electrons and positive ions, and the electron mean energy transport equations) is solved self-consistently coupled to Poisson's equation for the space-charge electrostatic field and the appropriated Maxwell's equations for the SW electromagnetic field. The model is solved for argon discharges over a broad range of operating conditions: Average electron densities from 10^{11} to 3×10^{12} cm^{-3} and gas pressures from 10^{-2} to 5 Torr. Results are compared to those of a simplified classical model that disregards charge separation near discharge boundaries, ignoring also the development of electron-plasma resonances caused by the severe electron density gradients within space-charge sheath regions. Simulations show that the presence of a sheath-resonance region has a strong influence on the values of the SW attenuation constant, particularly at low pressures and high electron densities, affecting also the local budget of the discharge power deposition (hence discharge maintenance).

DOI: 10.1103/PhysRevE.79.016403 PACS number(s): 52.80.Pi, 52.50.Sw, 52.40.Kh, 52.65.Kj

I. INTRODUCTION

Surface-wave (SW) plasmas produced by microwave discharges have been extensively investigated, both theoretically and experimentally, as reviewed in Refs. [1–9]. Recent studies on SW discharges [10–13] pointed out the role of plasma boundaries on the wave-plasma power coupling, through an interplay between the development of charge separation regions (termed space-charge sheaths) and local electron-plasma resonances. Charge separation within plasma sheaths is limited by a so-called space-charge (electrostatic) field. Its self-maintenance involves a considerable amount of energy transported from different discharge regions towards plasma boundaries (electrodes, walls), in order to compensate for the enhanced losses therein [14–16]. Electron-plasma resonances [17] develop in the vicinity of over-dense plasma boundaries wherever $\omega_p \simeq \omega$ (ω is the SW excitation frequency; $\omega_p=\sqrt{n_e e^2/\varepsilon_0 m_e}$ is the electron plasma frequency; e and m_e are the electron charge and mass, respectively; n_e is the electron density; and ε_0 the vacuum permittivity), due to the severe gradient of n_e in these regions. The development of resonances at $\omega_p \simeq \omega$ in SW plasmas (corresponding to an electron density $n_{e_{res}}=7.45\times10^{10}$ cm^{-3} at 2.45 GHz) has been theoretically analyzed in the past for both cylindrical and infinite planar configurations [18–24]. Indirect evidence of the existence of such resonances has been reported for SW discharges with various configurations and dimensions, using different experimental techniques: (i) Measuring a peak in the plasma-floating potential difference [25]; (ii) detecting and monitoring the localized resonance peak with the SW field, sometimes correlating this measurement with the observation of the electron density at resonance position [17,26–29]; (iii) observing an energetic population with the electron energy distribution function, measured near the quartz window of a large-area planar SW [30]; (iv) detecting high-energy electron fluxes with directional Langmuir probes [31–35]. A review of experiments and discussions about the existence of such resonances can be found in [36].

The sheath-resonance relationship is usually not accounted for in classical discharge models for SW-sustained plasmas. A considerable number of such models adopts a physical description that separates the two main features of the problem (electromagnetic and plasma production and maintenance), focusing exclusively on (i) the axial wave propagation and attenuation (together with the wave-plasma power transfer), considering a plasma density whose radial distribution either follows an imposed profile (usually of Bessel-type) [37,38] or is just assumed as uniform [20,39–50]; (ii) the structure of the electron energy distribution function [51–53], the calculation of electron rate coefficients [54–56], or the definition of a kinetic scheme responsible for plasma production [57–59], under the presence of a uniform microwave field. These (separated) approaches were recently upgraded in order to better describe the plasma production mechanisms in axially inhomogeneous SW discharge columns, by coupling an electromagnetic description to the kinetic models of atomic [60,61] and molecular [62–65] gases. However, the development of space-charge sheaths and their interplay with electron-plasma resonances is still not considered in these works. Self-consistent models including a radial description of the discharge [22,66–70] also avoid this issue, by neglecting the space-charge sheath region (assuming its thickness to be negligibly small or,

*llalves@ist.utl.pt
†Also at Instituto de Plasmas e Fusão Nuclear, Instituto Superior Técnico, Av. Rovisco Pais, 1049-001 Lisboa, Portugal.

equivalently, considering ambipolar conditions, even for pressures as low as tens of mTorr), and thus by stopping the problem description at the sheath edge defined by Bohm's criterion [71]. Because this criterion overestimates the boundary value of the electron density, the condition for resonance formation is never attained for typical radially averaged electron densities $\bar{n}_e \sim 10^{12}$ cm^{-3}. An exception to this are the works of Aliev *et al.* [22], of Zhang *et al.* [70], and of Pérès *et al.* [72,73]. The first work [22] solves a self-consistent (electromagnetic and kinetic) model for SW-sustained discharges in the presence of plasma resonances. However, ambipolar conditions are once again adopted and the results presented are not radially resolved, as a consequence of the spatial averaging associated to the nonlocal approach, used in solving the electron Boltzmann equation. The other works deal with the radial modeling of SW discharges, produced either by a coaxial structure [70] or by a magnetically confined cylindrical structure [72,73] (presenting also simulation results for a zero dc magnetic field), at low radially averaged electron densities ($\bar{n}_e \sim 5\times10^9$–$5\times10^{10}$ cm^{-3} in [70] and $\sim10^{10}$–10^{11} cm^{-3} in [72]). Although ambipolar conditions are also considered here, these authors report a plasma resonance phenomenon near the discharge wall, when the models run at very low $\bar{n}_e$ values. In both cases, however, the description of the wave-plasma energy coupling is still incomplete, because it neglects the formation of the space-charge sheath.

The work reported in this paper is an extension of the classical discharge models [66–70], providing the radial description of magnetic-free SW-sustained plasmas at low and moderate pressures. The update is mainly associated with the inclusion of space-charge sheath regions near discharge boundaries. This is achieved by developing a self-consistent, stationary radial model, which couples the classical model equations (charged particle transport equations and Maxwell's equations) to Poisson's equation (accounting for charge separation across the discharge), and to the nonlocal electron energy balance equation (accounting for energy transport and deposition, as to ensure sheath formation). The model is applied to the study of microwave discharges with cylindrical symmetry, produced in the absence of an external magnetic field by TM_{00} SWs within either a cylindrical or a coaxial structure. Notice that the one-dimensional (radial) description accounts for the maintenance of an axial plasma slice, which can be used afterwards to deduce the axial distribution of the plasma density [39,67].

Because our goal is the improvement of a discharge model for SW-sustained plasmas, the study will adopt a simplified kinetic scheme, considering electron collisions with ground-state atoms only. This decision has two direct consequences. First, by neglecting electron-neutral stepwise ionization processes, model predictions will overestimate the values of the electron mean energy. Second, by ignoring electron-electron collisions, the model also excludes calculating the electron energy distribution function (EEDF) from the solution to the electron Boltzmann equation. In fact, for microwave discharges running at 2.45 GHz with relatively high ionization degrees ($\gtrsim5\times10^{-4}$, for typical 30 mTorr gas pressure, 500 K gas temperature, and 2.5×10^{11} cm^{-3} electron density), and for the particular case of gases (such as argon) exhibiting a Ramsauer's minimum in its momentum-transfer cross section [74], electron-electron collisions can have a leading role in defining the electron distribution function. In this case it is preferable, and certainly closer to reality, to assume a Maxwellian EEDF [69,74], instead of calculating a nonequilibrium distribution function.

As mentioned, the formation of space-charge sheaths in SW plasmas, at low electron densities, is automatically linked to the development of electron-plasma resonances, due to the strong decrease in n_e down to the fulfillment of condition $\omega_p=\omega$, near discharge walls. In this case, the sheath and the resonance phenomena are inseparable, hence requiring a joint description, even if our main interest is with the study of charge separation regions. By itself, the revised formulation presented here immediately provides additional information about the radial structure of SW-sustained plasmas, allowing for a control upon the influence of space-charge sheaths in the local budget of discharge power. Moreover, the present model can add a contribution to the study of the sheath-resonance relationship, for example, by providing information about the relative positions of these structures, to be subsequently used in the construction of more detailed kinetic models.

The organization of this paper is the following. Section II presents the general formulation of the model, Sec. III details the description of resonance region, and Sec. IV summarizes the numeric procedures adopted. Model results, focusing on the comparison with predictions of a simplified classical model and the analysis of discharge power deposition, are presented in Sec. V and final remarks conclude in Sec. VI.

II. MODEL FORMULATION

The model developed here solves the stationary equations for the radial transport of charged particles with the plasma (obtained by calculating the moments of the corresponding kinetic Boltzmann equation), which are self-consistently coupled to Poisson's equation for the space-charge electrostatic field and the appropriated Maxwell's equations for the SW electromagnetic field. The moment model includes the continuity and the momentum-transfer equations for electrons and positive ions, and the electron mean energy transport equations, adopting the drift-diffusion approximation [16] for the electron particle and energy fluxes.

A. Framework

The model is applied to SW discharges in argon at frequency $\omega/2\pi=2.45$ GHz, pressures $p\simeq10^{-2}$–5 Torr, gas temperature $T_g=500$ K, and radially averaged electron densities $\bar{n}_e\simeq10^{11}$–3×10^{12} cm^{-3}. We consider two different excitation structures with cylindrical symmetry (a cylindrical structure and a coaxial structure), assuming in both cases that an azimuthally symmetric propagation mode develops in a plasma (of radius $R\simeq1$–10 cm), with electrons and positive ions. In the cylindrical structure [1,4,7,8] the plasma is surrounded by a dielectric glass tube with external radius $R_d > R$ and by an outer conductor with radius $R_{c,\mathrm{out}} > R_d$; in the coaxial structure [12,27,34,35,75,76] the plasma is created

between an inner antenna (metal rod with radius $R_{c,\mathrm{in}}$, surrounded by a layer of air with radius $R_v > R_{c,\mathrm{in}}$ and by a dielectric with radius $R_d > R_v$), and an outer conductor (radius $R > R_d$).

These work conditions validate the use of a stationary fluid description, as they yield $\omega \simeq 1.5 \times 10^{10}$ rad s$^{-1} \gg \nu_{\mathrm{eff}} \simeq 1.9 \times 10^7 - 2.7 \times 10^9$ s^{-1}, and $v_e/\nu_{\mathrm{eff}} \simeq 5.1 \times 10^{-3} - 3.7 \times 10^{-5}$ cm $\gg R \simeq 1-10$ cm (where $\nu_{\mathrm{eff}}/N \simeq 10^{-7} - 2.8 \times 10^{-8}$ cm^3 s^{-1}, according to pressure, is the effective electron-neutral collision rate coefficient [77,78] and $v_e \simeq 10^5$ cm s^{-1} is the electron drift velocity obtained from simulation results, see Sec. V A].

Another relevant issue to discuss is the nature of the electron heating phenomena involved in plasma maintenance. In SW discharges, these phenomena are usually associated to the collisional (Joule) heating under the action of the SW field. However, the fact that we are accounting for the development of (very intense) electron-plasma resonances introduces the possibility of electron heating due to noncollisional mechanisms in the oscillating field, such as (i) transit-time heating [19,79,80], associated to the change of the SW-field sharp peak during the transit-time interval τ of an electron across the resonance width Δ; (ii) resonance mode conversion, associated to the conversion of long-wavelength electromagnetic waves (with phase velocity $v_{\mathrm{ph}} \simeq c$, where c is the vacuum speed of light) into short-wavelength electrostatic electron-plasma waves [with phase velocity $v_{\mathrm{ph}} \simeq v_{\mathrm{th}} = (k_B T_e/m_e)^{1/2} \ll c$, where T_e is the electron temperature and k_B is the Boltzmann constant] [9,18,22,23,81], produced in the under-dense side of the sheath-resonance region (hence for $\omega^2 = \omega_p^2 + 3k^2 v_{\mathrm{ph}}^2 > \omega_p^2$, where k is the wave number), where they are easily absorbed by collisional or Landau damping.

According to our simulations, transit-time heating can probably become a relevant phenomenon only for intermediate pressures ($\sim$100 mTorr), in which case $\tau \simeq 2\pi/\omega$. At lower pressures the transit time is very small ($\tau \ll 2\pi/\omega$), because both the very thin resonance width and the high drift velocity contribute for an "instantaneous" electron transit across resonance region. At higher pressures the resonance width increases substantially and the electron drift velocity decreases, which leads to very long transit times satisfying $\tau \gg 2\pi/\omega$. In both these pressure regions, we expect electrons to interact only with an effective high-frequency field [55,68,78], gaining energy mainly through collisional heating. For this reason, the transit-time heating mechanism will not be considered here, although in Sec. V A we quantify the variation with pressure of the electron transit-time τ across resonance region. Resonance mode conversion involves a wave-plasma interaction inducing oscillations upon the electron density, and thus cannot be accounted for in the present stationary transport description.

Because of these limitations, we have controlled the physical coherence of the simulation results obtained within this framework. The procedure searches for a single value of the SW attenuation constant α, calculated by using two different (although complementary) descriptions: (i) Wave description, according to which α is obtained as an eigenvalue to the solution of Maxwell's equations; (ii) plasma description, which calculates α from the solution to the electron power balance equation. This convergence upon α is only achieved for an adequate description of resonance region, in terms of both the interval size and the number of grid points used in its numerical treatment, as will be shown in Sec. III.

B. Electron equations

The description of the electron particle and energy radial transport uses the corresponding continuity and flux equations [82]

$$\frac{1}{r}\frac{d}{dr}(r\Gamma_e) = n_e \nu_I, \tag{1a}$$

$$\Gamma_e = -n_e \mu_e E_s - \frac{d(n_e D_e)}{dr}, \tag{1b}$$

$$\frac{1}{r}\frac{d}{dr}(r\Gamma_\varepsilon) + \Gamma_e E_s + \Theta_{\mathrm{coll}} n_e = \mathrm{Re}[\sigma_p]/eE_{\mathrm{hf}}^2, \tag{1c}$$

$$\Gamma_\varepsilon = -n_e \varepsilon \mu_\varepsilon E_s - \frac{d(n_e \varepsilon D_\varepsilon)}{dr}. \tag{1d}$$

In these equations, Γ_e is the electron radial flux; ν_I is the electron ionization collision frequency; E_s is the electrostatic space-charge radial field; μ_e and D_e are the electron dc mobility and free-diffusion coefficient, respectively; ε is the electron mean energy; Γ_ε is the electron mean energy radial flux; Θ_{coll} is the power lost in collisions (elastic and inelastic) per electron; $\mathrm{Re}[\sigma_p]$ represents the real part of the plasma conductivity; E_{hf} is the root-mean-square of the total high-frequency (hf) electric field; μ_ε and D_ε are, respectively, the electron mobility and diffusion coefficient with the energy flux.

The description of the plasma energy absorption is given by the electron power balance equation (1c). The terms on its left-hand side (lhs) represent, respectively, the power lost (or gained) due to convection (energy flow following the radial transport of electrons in the discharge), including a term of drift under the action of the space-charge field and a (collisionless) pressure gradient term [79,83] [see Eq. (1d)]; the power lost in diffusion against the dc space-charge field (collisional cooling); and the power lost in friction due to electron-neutral collisions. Its right-hand side (rhs) represents the power gained from the SW field due to collisional heating, which is usually represented by the quantity $\Theta n_e \equiv \mathrm{Re}[\sigma_p]/eE_{\mathrm{hf}}^2$. Note that, in a classical local regime, the first two terms on the lhs of Eq. (1c) are neglected, as in this situation the energy acquired from the applied field is locally dissipated in collisions.

Equations (1a)–(1d) are directly obtained by integration, over all energies, of the radial-dependent electron Boltzmann equation written under the classical two-term approximation, which yields a drift-diffusion form for the corresponding particle and energy flux equations [16,82]. The expressions of the electron transport parameters and rate coefficients, as integrals of the electron distribution function, can be found elsewhere [82].

The model adopts the local mean energy approximation [16,84–89] (also termed nonlocal moment method, or just

described mentioning the use of look-up tables of the electron collision rates as a function of the electron mean energy), to introduce a radial dependence for the different electron parameters (EP). The procedure starts by tabulating, as a function of the electron mean energy, the different EP calculated from the corresponding EEDF. The table previously constructed is then used to map the EP in space by taking, for each position r, the value of the mean energy profile, $\varepsilon(r)$, as obtained from the solution to Eqs. (1c) and (1d) within the model. In the local mean energy approximation, the EP are assumed to bear the same relation to the space-dependent mean energy, as they do for the mean energy calculated from a homogenous EEDF. Therefore, this approximation accounts for the nonlocality of the electron particle and energy transport, allowing for a (indirect) modification of the EEDF, related to the spatial variation of the macroscopic electron density and mean energy. The local mean energy approximation can be used at low pressures ($p<0.1$ Torr), where it yields results in agreement with the popular nonlocal approach [15,90–98], and can be extended to high pressures ($p>1$ Torr), where it becomes equivalent to the local field approximation [84,99]. This latter approximation assumes that electrons are in local equilibrium with the applied electric field, hence that electron parameters can be parameterized as a function of this field, via the solution to the zero-dimensional (0D) electron Boltzmann equation. The homogenous EEDF used to implement the electron mean energy approximation can, in principle, be obtained from the solution to the homogeneous electron Boltzmann equation (written under the two-term approximation), for different electric field values. However, following the recommendations of Ref. [69], we will consider a Maxwellian EEDF, due to the increased influence of electron-electron collisions [74] in microwave discharges (i.e., for $\omega \gg \nu_{\mathrm{eff}}$) at high ionization degrees ($\gtrsim 5\times 10^{-4}$).

C. Ion equations

The description of the positive ion radial transport uses the corresponding continuity and momentum-transfer equations [100]

$$\frac{1}{r}\frac{d}{dr}(rn_p v_p) = n_e \nu_I, \tag{2a}$$

$$n_p v_p = -\frac{1}{\nu_p}\frac{1}{r}\frac{d}{dr}(rn_p v_p^2) + n_p \mu_p E_s, \tag{2b}$$

where n_p is the ion density, v_p is the ion radial drift velocity, μ_p is the ion mobility, and $\nu_p = e/m_p\mu_p$ is the ion-neutral momentum-transfer collision frequency (m_p is the ion mass). Equation (2b) is written in the cold ion approximation, which comes to neglect the diffusion term in the ion transport equations. In this approximation, Eqs. (2a) and (2b) present a singularity [101] at critical position $r=r_c$, where the ion drift velocity vanishes, i.e., $v_p(r_c)=0$. This singularity can be removed by introducing a regularity condition corresponding to zero space-charge field, i.e., $E_s(r_c)=0$. For the simple case of the (axis-symmetric) cylindrical structure this yields $r_c=0$, whereas for the coaxial structure the critical position is *a priori* unknown, constituting an eigenvalue to the problem.

D. Field equations

The radial distribution of fields is obtained by solving Poisson's equation for the electrostatic space-charge field

$$\frac{1}{r}\frac{d}{dr}(rE_s) = \frac{e}{\varepsilon_0}(n_p - n_e), \tag{3}$$

and Maxwell's equations for the TM_{00} mode of the SW electromagnetic fields [24]

$$\frac{d}{dr}(B_\varphi r) = j\frac{k_0^2}{\omega} r\varepsilon_i E_z, \tag{4a}$$

$$\frac{dE_z}{dr} = j\frac{\omega}{k_0^2}\frac{k^2}{r\varepsilon_i} B_\varphi r, \tag{4b}$$

$$E_r = -j\frac{\omega}{k_0^2}\frac{\gamma}{\varepsilon_i} B_\varphi. \tag{4c}$$

In these equations, B_φ is the azimuthal component of the magnetic field; E_z and E_r are, respectively, the axial and radial components of the electric field ($E_{\mathrm{hf}} \equiv \sqrt{E_r^2 + E_z^2}/\sqrt{2}$); ε_i is the relative permittivity of medium i ($\varepsilon_v = 1$ for air, $\varepsilon_d = 3.8$ for the dielectric glass, and $\varepsilon_i = \varepsilon_p$ for the plasma); $\gamma = \alpha + j\beta$ is the propagation constant (with α the SW attenuation constant and β its phase constant); and $k^2 \equiv k_0^2\varepsilon_i + \gamma^2$, with $k_0 \equiv \omega/c$.

The description of the wave-plasma energy coupling, including the formation of electron-plasma resonances, involves the self-consistent calculation of the plasma relative permittivity. The latter relates to the electron density radial profile via the classical dispersion relation [1–9]

$$\varepsilon_p = 1 + \frac{\sigma_p}{j\omega\varepsilon_0} \simeq 1 - \left(\frac{\omega_p}{\omega}\right)^2 - j\frac{\nu_{\mathrm{eff}}}{\omega}\left(\frac{\omega_p}{\omega}\right)^2, \tag{5}$$

where the last member was obtained in the so-called hf limit, for which $\omega \gg \nu_{\mathrm{eff}}$, yielding $\varepsilon_p \simeq 0$ for $\omega_p = \omega$ (or $n_{e_{\mathrm{res}}} = 7.45\times 10^{10}\ \mathrm{cm}^{-3}$ at $\omega/2\pi = 2.45$ GHz). Note that this zero-permittivity condition is in fact responsible for the development of a plasma resonance, as it can be confirmed by analyzing Eqs. (4b) and (4c). Further note that, in the coaxial structure, this condition is fulfilled twice in the radial direction, near both (dielectric and metal) plasma boundaries, leading to the formation of two electron-plasma resonances.

E. Boundary conditions and eigenvalues

In the cylindrical structure, boundary conditions for the transport equations include symmetry conditions at discharge axis [$dn_e/dr(0)=0$, $dn_p/dr(0)=0$, $d\varepsilon/dr(0)=0$, and $E_s(0)=0$], a zero-current condition at the plasma-dielectric boundary, $\Gamma_e(R) = n_p(R)v_p(R)$, and the imposition of the electron particle and mean energy fluxes at the same boundary

$$\Gamma_e(R) = \tfrac{1}{2} n_e(R)\langle v\rangle(R), \tag{6a}$$

$$\Gamma_\varepsilon(R) = \tfrac{1}{2} n_e(R)\langle uv\rangle(R), \tag{6b}$$

where $\langle v\rangle$ and $\langle uv\rangle$ represent the mean values of v and uv, respectively, calculated over the EEDF ($u=m_e v^2/2e$ is the electron kinetic energy in eV). In the coaxial structure, the set of boundary conditions include flux conditions similar to (6a) and (6b), imposed at both (dielectric and metal) boundaries limiting the plasma, the zero-current condition at the plasma-dielectric boundary, and regularity conditions at the critical position [$v_p(r_c)=0$, $E_s(r_c)=0$, and a closure relation for $n_p(r_c)$ [101] obtained from Eqs. (2a), (2b), and (3).

The boundary conditions for Maxwell's equations impose the continuity of the B_φ and E_z components at the interfaces of two different media, with the following limiting conditions: $B_\varphi(0)=0$ and $E_z(R_{c,\mathrm{out}})=0$, or $E_z(R_{c,\mathrm{in}})=0$ and $E_z(R)=0$, for the cylindrical or the coaxial structure, respectively.

Equations (1)–(5), subject to the previous boundary conditions, are solved for the excitation structures considered, given the radially averaged electron density $\bar{n}_e$ and the gas density $N=p/k_B T_g$, yielding the eigenvalues r_c (in the coaxial case), $E_{\mathrm{hf}}(0)/N$ or $E_{\mathrm{hf}}(R_{c,\mathrm{in}})/N$ (in the cylindrical or the coaxial case, respectively), and γ, together with the radial profiles of the charged particle densities [$n_e(r)$ and $n_p(r)$], fluxes [$\Gamma_e(r)$, $n_p(r)v_p(r)$, and $\Gamma_\varepsilon(r)$], mean energy $\varepsilon(r)$, and fields [$E_s(r)$ and $E_{\mathrm{hf}}(r)$].

F. Simplified model version

The results of the complete model developed here are compared to those obtained with a simplified model version, which adopts the approximations usually considered in the classical description of SW discharges [66–70]. In particular, the simplified model (i) neglects the sheath region, replacing the flux boundary condition (6a) by Bohm's criterion [71] $\Gamma_e(R)=n_e(R)v_s$, with $v_s \simeq (k_B T_e/m_p)^{1/2}$ the ion sound speed and T_e the electron kinetic temperature defined as $k_B T_e/e=(2/3)\varepsilon(0)$; (ii) imposes the quasineutral ambipolar conditions $n_p(r)=n_e(r)$ and $\Gamma_e(r)=n_p(r)v_p(r)$, disregarding both the ion continuity equation (2a) and Poisson's equation (3); (iii) adopts the local field approximation [84,99], instead of the local mean energy approximation, neglecting the convection and space-charge field terms in the electron energy transport equations (1c) and (1d). As a result, the radial dependence of the electron mean energy and the ionization frequency (the only EP for which a spatial variation is considered, in these simplified models) follows that of the applied SW field, $E_{\mathrm{hf}}(r)$.

As mentioned, the main goal with this paper is the update of classical SW discharge models. This is directly related to the use of assumptions (i)–(iii) in these models and to the strong impact that they have on simulation results, as will be shown in Sec. V.

III. RESONANCE DESCRIPTION

The self-consistent solution to the discharge model presented in Sec. II requires a specific description of resonance regions, in order to prevent the numerical problems associated with a rapid variation therein of parameters like the plasma permittivity or the SW electric field. As an answer to this problem, the Maxwell's equations for the B_φ and E_z field components are solved using a semianalytical approach, which starts by obtaining its solution under an integral-differential form [24]. In particular, Eqs. (4a) and (4b) are integrated over a region of width δ around the position of each resonance center r_{res} (at which $\mathrm{Re}[\varepsilon_p(r_{\mathrm{res}})]=0$), yielding

$$B_\varphi(r) = B_\varphi^0 - \frac{1}{r}\int_{r_0}^{r} r'\varepsilon_p(r')dr' \int_{r_0}^{r'} \frac{k^2(r'')}{\varepsilon_p(r'')} B_\varphi(r'')dr'', \tag{7a}$$

$$E_z(r) = E_z^0 + j\frac{\omega}{k_0^2}\int_{r_0}^{r} \frac{k^2(r')}{\varepsilon_p(r')} B_\varphi(r')dr', \tag{7b}$$

with $r_0 \equiv r_{\mathrm{res}} - \delta/2$. In these equations, B_φ^0 and E_z^0 are zero-order expressions for the magnetic and the axial-electric fields, respectively, given by

$$B_\varphi^0 = \frac{r_0}{r}\left(B_\varphi(r_0) + \frac{1}{r_0^2\varepsilon_p(r_0)}\frac{d}{dr}[rB_\varphi(r)]_{r_0}\int_{r_0}^{r} r'\varepsilon_p(r')dr' \right), \tag{8a}$$

$$E_z^0 = -j\frac{\omega}{k_0^2}\frac{1}{r_0\varepsilon_p(r_0)}\frac{d}{dr}[rB_\varphi(r)]_{r_0}. \tag{8b}$$

Equations (8a) and (8b) are used as initial conditions for the numerical iterative solution to Eqs. (7a) and (7b). In these equations, the second terms on the rhs are first-order corrections to the fields, for a resonance width assumed much smaller than the SW penetration length, i.e., $\delta \ll k^{-1}$.

Strictly, the interval size δ is a mathematical quantity, which does not necessarily correspond to the physical resonance width Δ, defined in classical propagation theory [21,102]. In this framework, the width Δ is obtained from a condensed expression of E_r (corresponding to the most intense component of the SW electric field), which captures its main features around r_{res}. At resonance, the behavior of E_r is mainly dependent on the plasma permittivity (5), whose real and imaginary parts can be essentially written as

$$\mathrm{Re}[\varepsilon_p(r)] \simeq a(r - r_{\mathrm{res}}), \tag{9a}$$

$$\mathrm{Im}[\varepsilon_p(r)] \simeq -s, \tag{9b}$$

with [for $\omega_p(r_{\mathrm{res}}) \simeq \omega$]

$$a \equiv \left.\frac{d(\mathrm{Re}[\varepsilon_p])}{dr}\right|_{r_{\mathrm{res}}} \simeq \left|\frac{(dn_e/dr)_{r_{\mathrm{res}}}}{n_e(r_{\mathrm{res}})}\right|, \tag{10a}$$

$$s \equiv \frac{\nu_{\mathrm{eff}}(r_{\mathrm{res}})}{\omega}. \tag{10b}$$

Therefore, in resonance region, Eq. (4c) for the radial component of the SW electric field becomes [see also Eqs. (7a) and (8a)]

$$E_r(r) \simeq \frac{AB_\varphi(r_{\rm res})(r_{\rm res}/r)}{a(r-r_{\rm res})-js}, \tag{11}$$

where $A \equiv -j\gamma(\omega/k_0^2)$. The resonance width Δ is then defined as the full width at half-maximum (FWHM) associated to the square of the electric field amplitude

$$\left| E_r\left(r_{\rm res}+\frac{\Delta}{2}\right)\right|^2 = \frac{|E_r(r_{\rm res})|^2}{2}, \tag{12}$$

which gives (for $\Delta/r_{\rm res} \ll 1$)

$$\Delta = 2\frac{\nu_{\rm eff}(r_{\rm res})}{\omega}\left|\frac{n_e(r_{\rm res})}{(dn_e/dr)_{r_{\rm res}}}\right|. \tag{13}$$

Numerically, the interval(s) δ is (are) calculated as to provide a description of resonance(s) (one or two, for the cylindrical or the coaxial structure, respectively) that ensures electron power conservation. In particular, we adopt an iterative procedure upon the SW attenuation constant α, that changes both the interval(s) δ and the number of grid points used in the numerical treatment of resonance region. Convergence searches for a single value of α, obtained either as an eigenvalue to Maxwell's equations (7a), (7b), (8a), and (8b) or from the electron power balance equation using [39,44–46,67]

$$\alpha = \frac{1}{2}\frac{dP_{\rm gain}/dz}{P_{\rm inc}} \equiv \frac{1}{2}\frac{\int_{\rm plasma} {\rm Re}[\sigma_p]/eE_{\rm hf}^2 2\pi r dr}{\frac{\varepsilon_0 c^2}{4e}\int_{\rm structure}[E_r B_\varphi^\star + E_r^\star B_\varphi]2\pi r dr}. \tag{14}$$

The numerator of Eq. (14), $dP_{\rm gain}/dz$, is the total power, per unit length, absorbed by the plasma [see Eq. (1c)], whereas its denominator, $P_{\rm inc}$, represents the local incident power upon a discharge cross section (the superscript * accounts for the conjugate complex). As an example, Fig. 1 plots α as a function of δ/R, for different numbers of grid points $N_{p,\rm res}$ within resonance region. Results were obtained for a discharge produced at 100 mTorr pressure and 10^{12} cm^{-3} average electron density, in a cylindrical structure (R=0.8 cm, R_d=0.95 cm, and $R_{c,\rm out}$=5 cm). As shown, the match between the calculations of α, using either a wave description or a plasma description, is ensured only for a correct combination of δ and $N_{p,\rm res}$ values, for example, adopting $\delta/R = 8\times10^{-4}$ and $N_{p,\rm res}$=100 in the conditions of Fig. 1. With this formulation, the SW attenuation constant becomes the key parameter for the description of the wave-plasma energy coupling, providing also a way to check the physical coherence of model results.

IV. NUMERICS

The fluid equations (1)–(3) are discretized using a second-order finite difference representation in a nonuniform grid, with local grid refinement near the integration boundary(ies). Due to the severe gradients in these regions, the flux equations (1b) and (1d) are discretized following the Scharfetter-Gummel exponential scheme [103]. The solution to the fluid equations adopts a leapfrog method, combined with a Newton-Raphson algorithm to linearize the ion transport equations (2a) and (2b). The solution to Maxwell's equations (4a)–(4c) adopts a fourth-order Runge-Kutta implicit method, outside resonance region(s), shifting to the semianalytic procedure described in Sec. III, for a region of width δ around each resonance center. The interval(s) δ, together with a local grid refinement within resonance region(s), are iteratively calculated as to ensure the same value of α, obtained either as an eigenvalue to Maxwell's equations or from the electron power balance equation (see Sec. III). Eigenvalues calculation involves a combination of bisection and Newton-Raphson methods. Figure 2 presents the flowchart of the calculation scheme adopted. Notice that the determination of eigenvalue $E_{\rm hf}(0)/N$ [or $E_{\rm hf}(R_{c,\rm in})/N$ in the coaxial case] uses a two-step procedure, which involves the normalization of the electron mean energy profile to some reference value, for example $\varepsilon(r_c)$ at critical point.

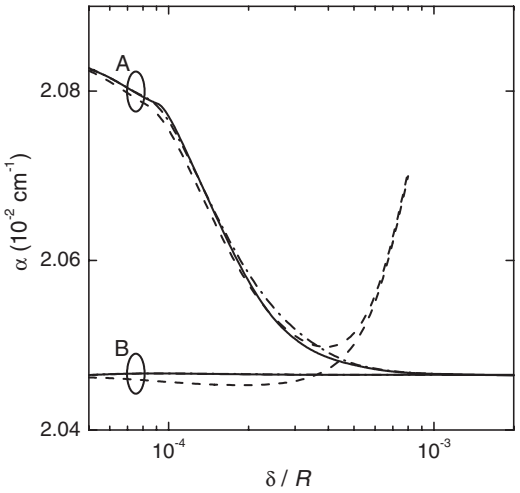

FIG. 1. Surface-wave attenuation constant α, as a function of δ/R, for a cylindrical structure (R=0.8 cm, R_d=0.95 cm, and $R_{c,\rm out}$=5 cm), at $\bar{n}_e = 10^{12}$ cm^{-3} and p=100 mTorr. Results were obtained by calculating α as an eigenvalue to Maxwell's equations (curves A) or from the electron power balance equation (B), for the following number of grid points $N_{p,\rm res}$: 100 (solid curves), 10 (dashed curves), and 1000 points (dashed-dotted curves).

The model is solved in a $10^3-5\times10^3$ points grid, for minimum relative step sizes between $10^{-6}-10^{-7}$. The convergence test is applied to the profiles of all calculated quantities and to the eigenvalues, checking for relative errors smaller than 10^{-8}.

V. RESULTS AND DISCUSSION

The model adopts the direct electron cross-sections set deduced in Ref. [104] and the ion-neutral momentum-transfer collision frequency of Ref. [105]. As mentioned, we consider two different excitation structures with the following geometrical dimensions: R=0.8 cm, R_d=0.95 cm, and $R_{c,\rm out}$=5 cm (for the cylindrical structure); $R_{c,\rm in}$=0.5 cm, R_v=1.34 cm, R_d=1.5 cm, and R=7.5 cm (for the coaxial structure).

A. Results for the cylindrical structure

The model is applied to the cylindrical structure considered, in view of a systematic analysis of the main features

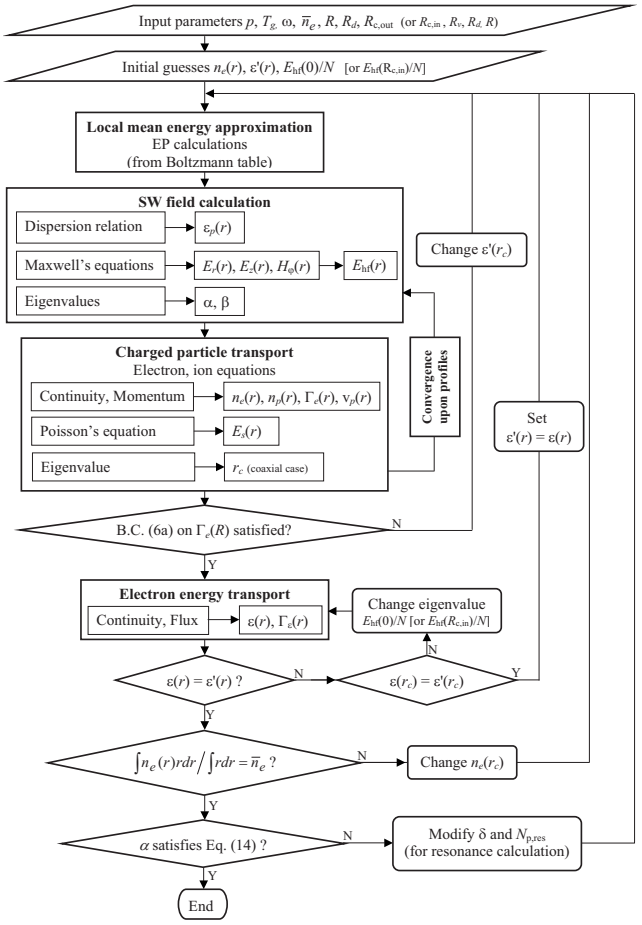

FIG. 2. Flowchart of the calculation scheme for the modeling of SW discharges with cylindrical symmetry. The information in parentheses refers to calculations in the coaxial structure. The critical position r_c is set equal to zero for calculations in the cylindrical structure.

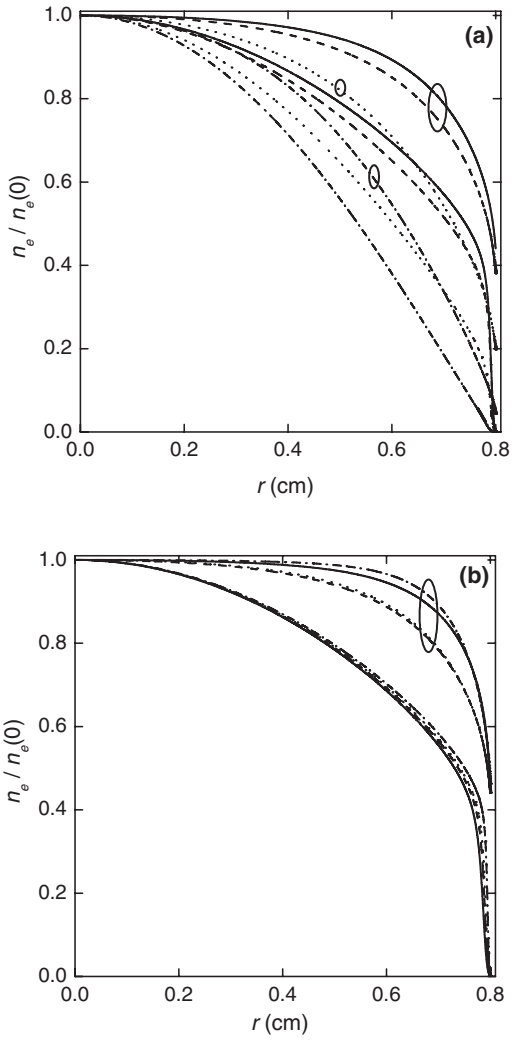

FIG. 3. Radial profiles of the reduced electron density $n_e/n_e(0)$, for the cylindrical structure at different work conditions. Results were obtained using the model developed here (plain curves) and a simplified model version that neglects the sheath region (curves marked with circles). (a) Results for $\bar{n}_e=10^{12}$ cm^{-3} and the following values of p (in Torr) [corresponding to the following values of $n_e(0)$ (in cm^{-3}), as calculated with the complete model]: 0.03 [$n_e(0)=1.4\times10^{12}$] (solid curves); 0.1 [1.5×10^{12}] (dashed curves); 0.5 [1.8×10^{12}] (dotted curves); 5 [2.2×10^{12}] (dashed-dotted curves). (b) Results for $p=30$ mTorr and the following values of $\bar{n}_e$ (in cm^{-3}) [corresponding to the following values of $n_e(0)$ (in cm^{-3}), as calculated with the complete model]: 4×10^{11} [$n_e(0)=5.8\times10^{11}$] (solid curves); 7×10^{11} [1.0×10^{12}] (dashed curves); 10^{12} [1.4×10^{12}] (dotted curves); 3×10^{12} [4.2×10^{12}] (dashed-dotted curves).

characterizing both the sheath-resonance region and the discharge power deposition.

1. General characteristics

Figures 3(a) and 3(b) show the profiles of the reduced electron density $n_e/n_e(0)$, calculated using both the complete model developed here and its simplified version, at $\bar{n}_e=10^{12}$ cm^{-3} for $p=0.03, 0.1, 0.5, 5$ Torr and $p=30$ mTorr for $\bar{n}_e=4\times10^{11}$, 7×10^{11}, 10^{12}, 3×10^{12} cm^{-3}, respectively. From the results in these figures one observes that the electron density gradient near the dielectric boundary is severely limited when the sheath region is neglected (as in the simplified model version), and that this effect is more noticeable at low pressure regardless of $\bar{n}_e$. Moreover, the electron density profiles are strongly affected by pressure variations (exhibiting a less homogeneous shape at high p), whereas they are much less dependent on $\bar{n}_e$. This behavior is related to a reduction in the electron flux as the pressure increases, which can be confirmed from Figs. 4(a) and 4(b) that show the profiles of $\Gamma_e/n_e(0)$ for the same conditions as before. An observation of these figures also reveals that, despite the differences in the calculated electron flux profiles obtained with the complete and the simplified models, both approaches yield similar results for the boundary value $\Gamma_e(R)/n_e(0)$ at low pressures (for all average densities considered here).

The difference between the results obtained with the complete and the simplified models can also be observed in Figs. 5(a) and 5(b), which show the profiles of the electron mean energy for various pressures at $\bar{n}_e=10^{12}$ cm^{-3} and for various average electron densities at $p=30$ mTorr, respectively. The quasihomogeneous profiles obtained with the complete model, which accounts for the nonlocal energy transport, are

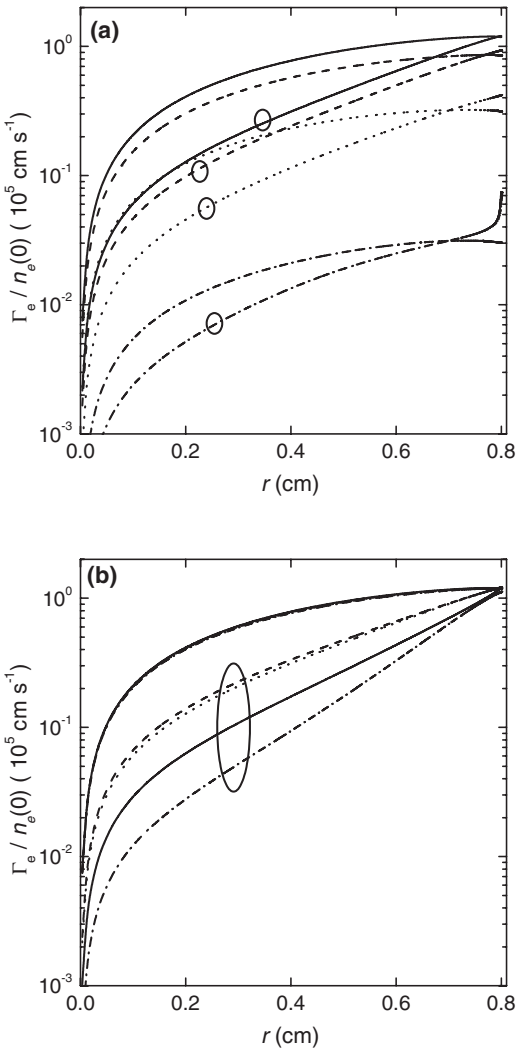

FIG. 4. Radial profiles of the reduced electron flux $\Gamma_e/n_e(0)$, for the same conditions of Fig. 3.

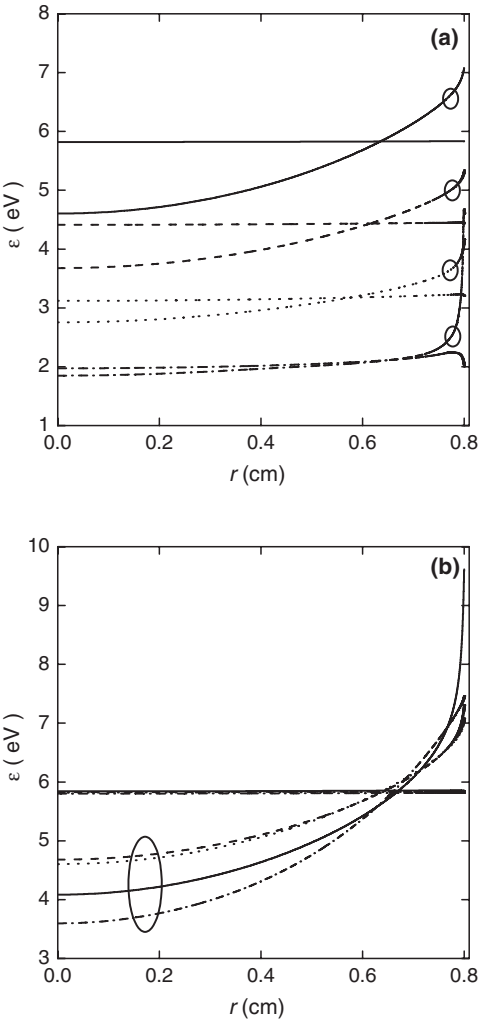

FIG. 5. Radial profiles of the electron mean energy ε, for the same conditions of Fig. 3.

in contrast with the radial increase in ε, induced by the local field approximation adopted in the simplified model. These differences are especially important at low pressures, although they are still very significant at high pressures near the dielectric wall [see Fig. 5(a)]. Moreover, the mean energy profiles calculated with the complete model are little affected by variations in the average electron density, contrarily to those obtained with the simplified model [see Fig. 5(b)]. Notice that the poor quality of the mean energy profiles calculated with the simplified model leads to a deficient description of the electron production and transport, as observed in Figs. 3 and 4. However, as expected, both models yield higher electron mean energies at low pressures, to compensate for the higher losses of charged particles under these conditions.

Figure 6(a) shows the radial distribution (across the cylindrical structure) of the SW electromagnetic field components E_r, E_z, and $H_\varphi \equiv \varepsilon_0 c^2 B_\varphi$ (the latter multiplied by a factor of 10^3), normalized to $E_z(0)$, at $\bar{n}_e = 10^{12}$ cm^{-3} and $p = 100$ mTorr (corresponding to a calculated incident power $P_{\text{inc}} \simeq 180$ W). For the same conditions, Fig. 6(b) plots the radial profiles (across the plasma) of the total reduced hf field E_{hf}/N, and the reduced electron density $n_e/n_e(0)$. One notes the resonance peaks of the applied fields near the dielectric wall (at $r = 0.8$ cm), due to the rapid variation of the electron density (thus, of the plasma permittivity) in this region [see the inset in Fig. 6(b), where the horizontal dotted line marks the value of the electron density $n_{e_{\text{res}}}$].

Figures 7(a), 7(b), 8(a), and 8(b) present, as a function of the radial position across the plasma, the SW electric field components E_r and E_z [normalized to $E_z(0)$], calculated using both the complete model developed here and its simplified version, at $\bar{n}_e = 10^{12}$ cm^{-3} for $p = 0.03$, 5 Torr and $p = 30$ mTorr for $\bar{n}_e = 4 \times 10^{11}$, 3×10^{12} cm^{-3}, respectively. Because Bohm's criterion overestimates the boundary value of the electron density, the condition for resonance formation is not attained when using the simplified model, as can be observed from the results in these figures [see, in particular, the insets in Figs. 7(a) and 8(a)]. In general, and for the range of values analyzed here, the amplitude of both electric field components increases with pressure (at constant $\bar{n}_e$), but only that of the axial component increases with the average electron density (at constant p). Figures 7 and 8 show also that the resonance peak becomes wider (and simultaneously less

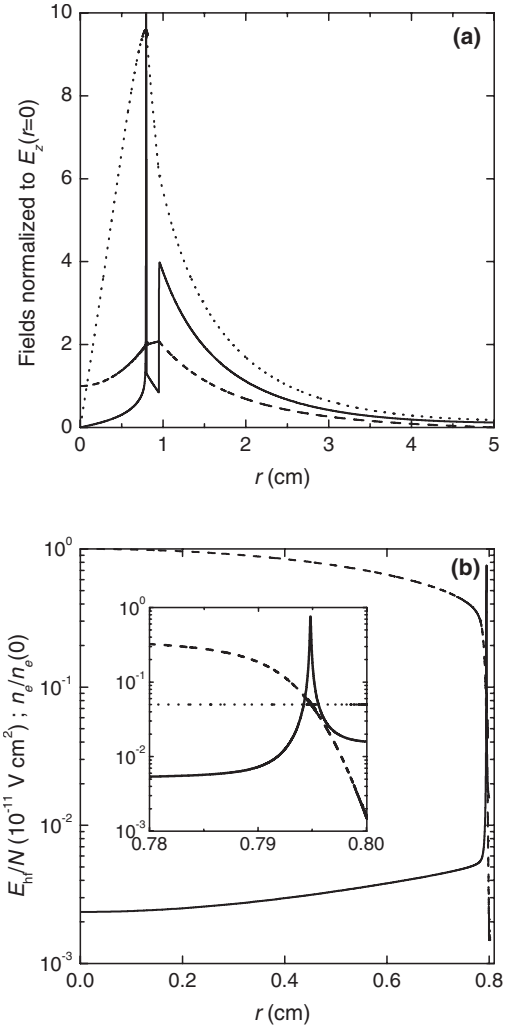

FIG. 6. (a) Radial distribution (across the cylindrical structure) of the SW electromagnetic field components, normalized to $E_z(0)$, at $\bar{n}_e=10^{12}$ cm^{-3} and $p=100$ mTorr (corresponding to $n_e(0)=1.5\times10^{12}$ cm^{-3}): E_r (solid curve); E_z (dashed curve); $H_\varphi\times1000$ (dotted curve). (b) Radial profiles (across the plasma) of the total reduced hf field E_{hf}/N (solid curve), and the reduced electron density $n_e/n_e(0)$ (dashed curve), for the same conditions of Fig. 6(a). The inset is a blowup of this figure, over sheath region, where the horizontal dotted curve is for $n_{e_{res}}=7.45\times10^{10}$ cm^{-3}.

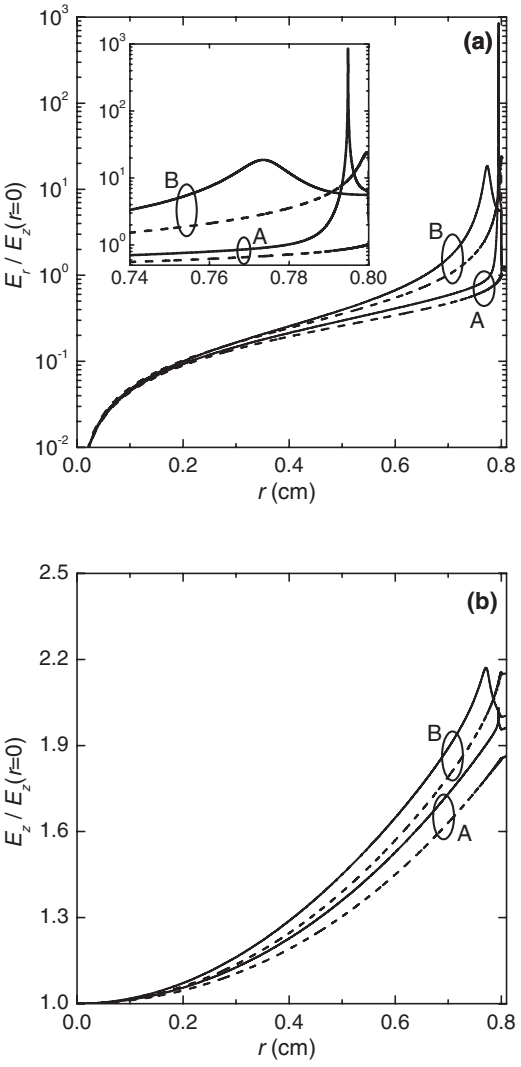

FIG. 7. Radial distribution (across the plasma) of the SW electromagnetic field components, $E_r/E_z(0)$ (a) and $E_z/E_z(0)$ (b), for the cylindrical structure at $\bar{n}_e=10^{12}$ cm^{-3} and the following values of p (in Torr): 0.03 (curves A); 5 (B). Results were obtained using the model developed here (solid curves) and a simplified model version that neglects the sheath region (dashed curves). The inset in Fig. 7(a) is a blowup of this figure over sheath region.

intense) for either an increase in pressure (hence in the electron-neutral collision frequency) or a decrease in the average electron density (hence in the electron density gradient near the wall) [see the insets in Figs. 7(a) and 8(a)], thus reproducing the behavior predicted by the theoretical expression of the resonance width [see Eq. (13)]. In addition, there is a perfect agreement between the values of Δ, calculated either analytically from Eq. (13) or numerically by estimating the FWHM of the resonance peak from simulations, which confirms the coherence of model results. As an example, Fig. 9 plots Δ vs p at $\bar{n}_e=10^{12}$ cm^{-3}, as obtained using both calculation methods. As mentioned, the resonance width Δ does not correspond to the interval size δ. Simulation results show that the ratio Δ/δ can vary from 10^{-2} at low pressures up to 10 at high pressures.

The position of the resonance relative to the nearby space-charge sheath is an important issue, which relates to the specific features of energy absorption by the plasma, whose knowledge can aid the construction of detailed kinetic models describing these structures. For example, it can provide relevant information for the so-called nonlocal kinetic model (or nonlocal approach) [90–98], concerning the turning point of the different electrons, i.e., the position at which they are reflected by the space-charge potential. Notice that this nonlocal approach applies only to confined electrons, whose total energy is lower than the wall potential, for which a spatial averaging procedure can be applied to the isotropic component of the corresponding Boltzmann equation, at low pressures ($p<0.1$ Torr). Therefore, the knowledge of the relative sheath-resonance position can be used to define the confinement boundary condition with the nonlocal kinetic model.

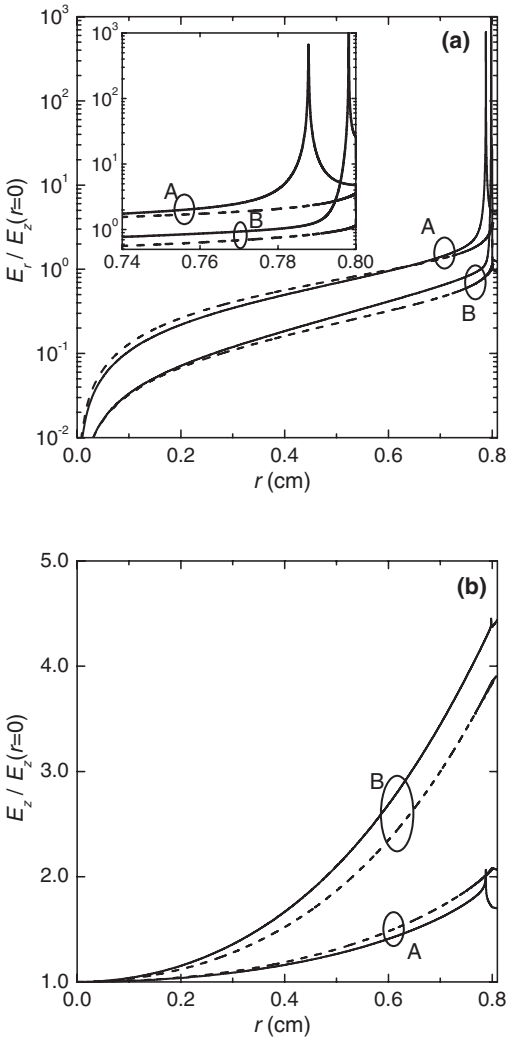

FIG. 8. As in Fig. 7, but for $p=30$ mTorr and the following values of $\bar{n}_e$ (in cm^{-3}): 4×10^{11} (curves A); 3×10^{12} (B).

With this respect, Figs. 7 and 8 seem to show that the resonance position shifts towards the corresponding plasma boundary whenever the pressure decreases or the electron density increases. Although this observation holds for $\bar{n}_e$ variations (regardless of p), it is violated when p varies within a range below 100 mTorr (probably due to the development of extended plasma sheaths at lower pressures). In any case, if the location of a resonance is easily identified with the position $r_{\rm res}$ of its center (where $\mathrm{Re}[\varepsilon_p]=0$), any attempt to define the exact place where a space-charge sheath begins (or, alternatively, its thickness with respect to the nearby boundary) is a subject of controversy. Therefore, the purpose here is just to work out some criterion allowing to separate the quasineutral plasma core from its charged periphery region. We have chosen to base our analysis upon the modifications (both in intensity and shape) of the space-charge field radial profiles, due to a variation in the discharge operating conditions (see Fig. 10, obtained at $\bar{n}_e=10^{12}$ cm^{-3} for various pressures). The idea is to produce a contour map with isointensity curves of E_s, along each of which the space-charge field has a given relative value η. In the particular case of this cylindrical structure, and for the set of

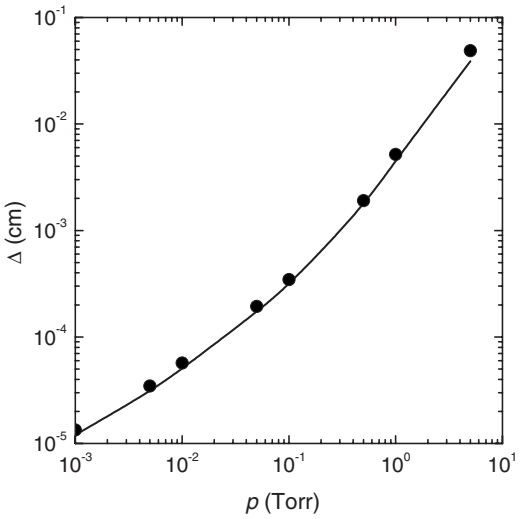

FIG. 9. Resonance width Δ, as a function of pressure, for the cylindrical structure at $\bar{n}_e=10^{12}$ cm^{-3}. The values were obtained from calculations, using Eq. (13) (solid curve) or the numerical simulation of the resonance peak (points).

pressure values considered in Fig. 10, we have defined η according to

$$\eta \equiv \frac{E_s(r_{\mathrm{sh},\eta})}{E_s(R)_{p=10\ \mathrm{mTorr}}}, \tag{15}$$

where $r_{\mathrm{sh},\eta}$ (which can be interpreted as the sheath edge position) is the radial position for a η intensity of E_s; and the denominator is a reference value of E_s, obtained at the dielectric wall and for 10 mTorr pressure. Applying Eq. (15) to the set of profiles plotted in Fig. 10, one obtains different isointensity contour lines of E_s, for different values of η, representing the evolution with pressure of the sheath edge $r_{\mathrm{sh},\eta}$. The results are shown in Fig. 11, together with the

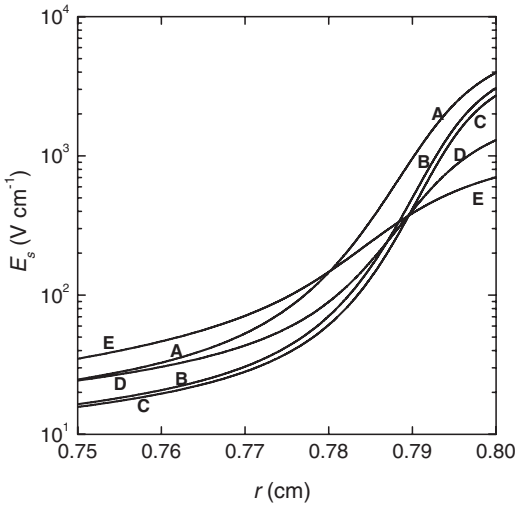

FIG. 10. Radial profiles of the space-charge field E_s (near the dielectric wall), for the cylindrical structure at $\bar{n}_e=10^{12}$ cm^{-3} and the following values of p (in Torr): 0.01 (curve A); 0.05 (B); 0.1 (C); 1 (D); 5 (E).

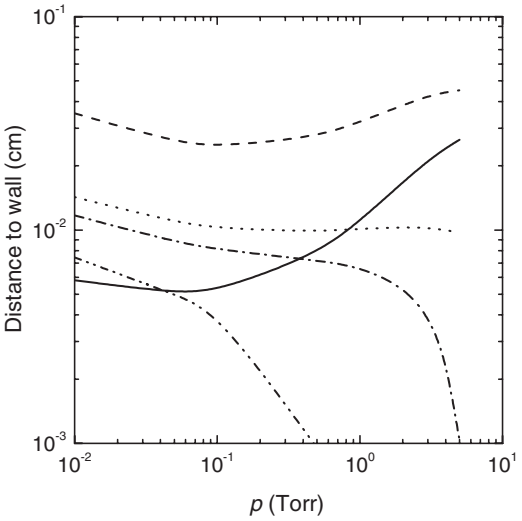

FIG. 11. Distance to the dielectric wall, as a function of pressure, of the resonance center (solid curve) and the sheath edge, defined using the following values of η [(see Eq. (15)]: 1% (dashed curve); 10% (dotted curve); 17% (dashed-dotted curve); 40% (dashed-dotted-dotted curve). Results were obtained for the cylindrical structure at $\bar{n}_e = 10^{12}$ cm^{-3}.

resonance position, in terms of distances to the dielectric wall. By analyzing this figure one concludes that, for pressures around 10 mTorr (at $\bar{n}_e = 10^{12}$ cm^{-3}), the resonance is unequivocally found inside the space-charge sheath, for all values of η used in the criterion adopted here. Numerical simulations show that this result holds for average electron densities above 10^{12} cm^{-3} (hence smaller distances $R - r_{\mathrm{res}}$), as E_s is less modified by variations in $\bar{n}_e$ than in p.

The self-consistent calculation of the attenuation constant α and the phase constant β is also strongly affected by the inclusion of the space-charge sheath region in SW discharge models. Figures 12(a) and 12(b) plot α and β, respectively, as a function of p for $\bar{n}_e = 7 \times 10^{11}$, 3×10^{12} cm^{-3}, whereas Figs. 13(a) and 13(b) present the phase curves of α and β, respectively, as a function of $\bar{n}_e$ for $p = 30$ mTorr. As before, the results depicted in these figures were obtained using the complete model developed here and its simplified version that neglects the sheath region (for $\bar{n}_e$ values that ensure $\omega_p > \omega$, thus disregarding also the electron-plasma resonance phenomenon). In general, the values of the attenuation constant obtained with the complete model are above those predicted by the simplified model. These deviations increase at low pressures and high electron densities [see Figs. 12(a) and 13(a)], probably due to the enhanced influence of the sheath-resonance phenomena upon the energy absorption by the plasma. In particular, notice that the simplified (classical) model yields a continuous increase in α with p, due to an enhancement of the collisional energy transfer, in contrast with the less monotonic evolution predicted by the complete model. Notice also that both models give similar results for the behavior of the phase constant with either the pressure or the average electron density, although yielding some

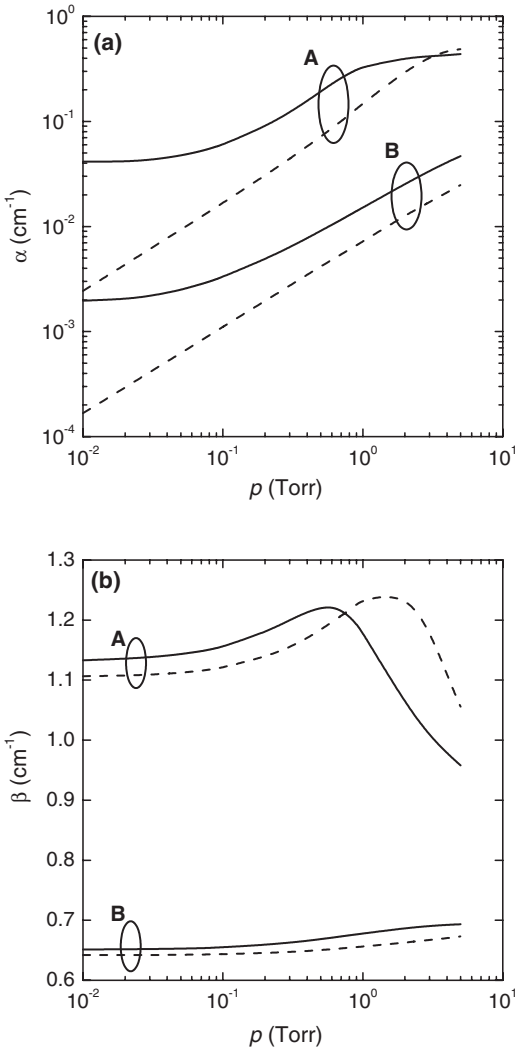

FIG. 12. Surface-wave propagation constants, α (a) and β (b), as a function of p, for the cylindrical structure at the following values of $\bar{n}_e$ (in cm^{-3}): 7×10^{11} (curves A); 3×10^{12} (*B*). Results were obtained using the model developed here (solid curves) and a simplified model version that neglects the sheath region (dashed curves).

dephasing for the evolution of β with p at low $\bar{n}_e$ [see Figs. 12(b) and 13(b)].

2. Energy balance

The results in the preceding section suggest that power deposition in SW discharges is strongly dependent on resonance features. This can be confirmed by analyzing Figs. 14(a) and 14(b) that plot the fractional local power transfer, as a function of radial position, at $\bar{n}_e = 10^{12}$ cm^{-3} and $p = 10$, 100 mTorr [Fig. 14(b) is simply a zoom of Fig. 14(a), over the sheath-resonance region]. The values of the power transferred from/to each channel (A)–(D) were obtained by calculating the contribution of the different terms of Eq. (1c), relative to the total power per unit length absorbed by the plasma, dP_{gain}/dz [see Eq. (14)]. Figure 14 is to be analyzed simultaneously with Fig. 15 representing, for the same conditions, the reduced electron mean energy flux $\Gamma_\varepsilon / n_e(0)$, as a

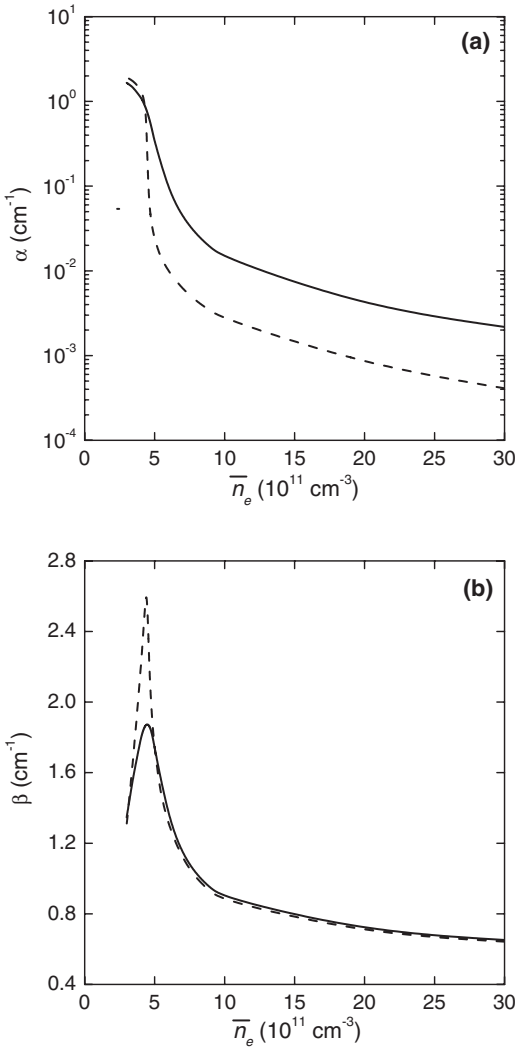

FIG. 13. Surface-wave phase curves of α (a) and β (b) as a function of $\bar{n}_e$, for the cylindrical structure at $p=30$ mTorr. Results were obtained using the model developed here (solid curves) and a simplified model version that neglects the sheath region (dashed curves).

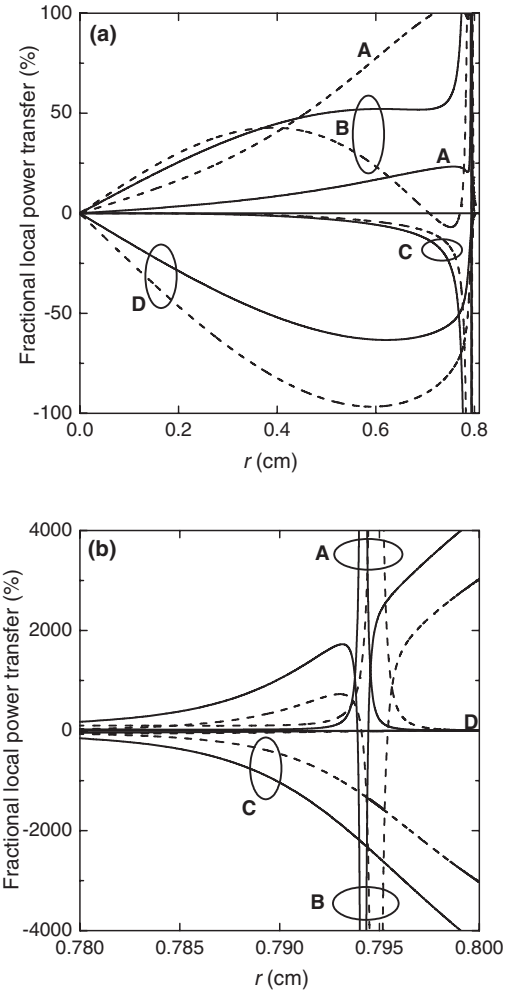

FIG. 14. (a) Fractional local power transfer, as a function of r, for the cylindrical structure at $\bar{n}_e=10^{12}$ cm^{-3} and the following values of p (in mTorr): 10 (solid curves), 100 (dashed curves). The different labels correspond to the following power transfer channels [see Eq. (1c)]: Collisional heating from the SW field (A); convection flow (B); collisional cooling in diffusion against the space-charge field (C); friction due to elastic and inelastic collisions (D). The positive (negative) values indicate a power gained (lost) by the electrons. Percentages were calculated relative to the total (radially integrated over a discharge cross section) power, per unit length, absorbed by the plasma. (b) Zoom of Fig. 14(a) over sheath-resonance region.

function of position. As shown in these figures, the energy absorbed by the electrons within the plasma resonance is radially transported in two opposite directions: Towards the discharge axis (corresponding to $\Gamma_\varepsilon<0$) where it is first used to build the plasma-sheath edge, after which is dissipated in collisions; towards the wall (corresponding to $\Gamma_\varepsilon>0$) where it is mainly used to maintain the space-charge field. In this sense, the combined action of resonance and convection phenomena promotes the distribution of energy, within (at least) the discharge cross section, in a way that strongly depends on pressure. At high pressures, when the resonance peak is less intense (see Figs. 7 and 9), the energy transfer is controlled by the classical mechanism of friction due to collisions [see the increased energy loss region associated to dashed curve D, in Fig. 14(a)]. At low pressures, however, the transfer of energy becomes strongly influenced by absorption in the resonance region [and subsequent transport due to convection; see the enhanced energy gain region associated to solid curve B, in Fig. 14(b)]. In this case the sharper resonance peak enters the charge separation region, setting up an enhanced sheath-resonance energy transfer.

Simulation results can also provide information about the energy gained by electrons from the SW field, within resonance region, due to both collisional heating $\varepsilon_c^{\mathrm{res}}$ and noncollisional (transit-time) heating $\varepsilon_{nc}^{\mathrm{res}}$, even if the latter is not considered in the model developed here. An estimation of these energies can be obtained using [notice that $E_r(r_{\mathrm{res}}) \simeq E_{\mathrm{hf}}(r_{\mathrm{res}})$]

$$\varepsilon_c^{\mathrm{res}} \simeq \frac{\mathrm{Re}[\sigma_p(r_{\mathrm{res}})]}{e n_e(r_{\mathrm{res}})} E_{\mathrm{hf}}^2(r_{\mathrm{res}})\tau, \tag{16a}$$

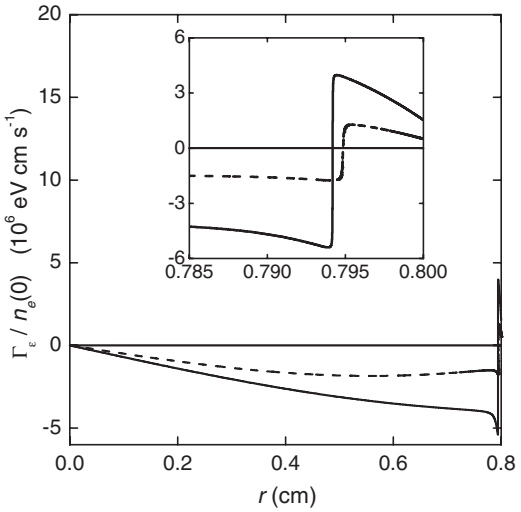

FIG. 15. Radial profile of the reduced electron mean energy flux $\Gamma_\varepsilon/n_e(0)$, for the same conditions of Fig. 14. The inset is a blowup of this figure over sheath-resonance region.

$$\varepsilon_{nc,\max}^{\mathrm{res}} \simeq \frac{E_{\mathrm{hf}}(r_{\mathrm{res}})}{2}\Delta, \tag{16b}$$

where $\tau \equiv \max(\tau_{\mathrm{dc}}, \tau_{\mathrm{hf}})$ is the electron transit time through the resonance due to either dc or hf transport phenomena, with

$$\tau_{\mathrm{dc}} \simeq \frac{\Delta}{v_{e_{\mathrm{dc}}}(r_{\mathrm{res}})} = \frac{\Delta}{\Gamma_e(r_{\mathrm{res}})/n_e(r_{\mathrm{res}})}, \tag{17a}$$

$$\tau_{\mathrm{hf}} \simeq \frac{\Delta}{v_{e_{\mathrm{hf}}}(r_{\mathrm{res}})} = \frac{\Delta}{\mathrm{Re}[\sigma_p(r_{\mathrm{res}})]/[en_e(r_{\mathrm{res}})]E_{\mathrm{hf}}(r_{\mathrm{res}})}. \tag{17b}$$

Notice that $\varepsilon_c^{\mathrm{res}}/\tau = \Theta(r_{\mathrm{res}})$ gives the rhs of Eq. (1c), per electron at resonance position, and that $\varepsilon_{nc,\max}^{\mathrm{res}}$ represents the total potential energy stored in the resonance peak, hence corresponding to the maximum energy that electrons can gain by noncollisional transit-time heating.

Table I presents estimations of these quantities at $\omega/2\pi = 2.45$ GHz, for $p = 0.01, 0.1, 5$ Torr and $\bar{n}_e = 7 \times 10^{11}, 10^{12}, 3 \times 10^{12}$ cm^{-3}. For comparison purposes we give also the values of the electron mean energy ε and the dc potential drop across the plasma ΔV_s (associated to the space-charge electrostatic field), the latter mainly due to the potential variation within sheath region. The results in this table confirm that, for the $\bar{n}_e$ values considered here, $\tau_{\mathrm{hf}} \ll \tau_{\mathrm{dc}} \ll 2\pi/\omega$ at low pressures (as in this case the very thin resonance is crossed by electrons with a very high drift velocity) and that $2\pi/\omega \ll \tau_{\mathrm{hf}} \ll \tau_{\mathrm{dc}}$ at high pressures (as in this case the large resonance is crossed by electrons with a low drift velocity). These observations also show that noncollisional transit-time heating can only become a relevant energy gain mechanism for pressures around hundreds of mTorr (see Sec. II A). Moreover, Table I reveals that $\varepsilon_c^{\mathrm{res}} \gg \varepsilon_{nc,\max}^{\mathrm{res}}$, which shows the importance of the collisional heating mechanism, and that $\varepsilon_c^{\mathrm{res}} \gg \varepsilon$, which confirms the role of transport in the discharge energy budget. Notice also that $\varepsilon_c^{\mathrm{res}} \simeq \Delta V_s$ at low pressures, because in this case the (local) energy gained is mainly used to build the space-charge sheath, whereas $\varepsilon_c^{\mathrm{res}} \gg \Delta V_s$ at high pressures, because in this case electron-neutral collisions become the main energy loss mechanism.

To complement the study of the discharge energy absorption, one can also analyze the distribution features of the total (radially integrated over a discharge cross section) power transfer, for various operating conditions. Figure 16 represents, as a function of NR, the fraction of total power lost by electrons, due to the various energy absorption channels considered: Convection, collisional cooling, and friction. The curves in this figure were obtained by radial integration of the different power loss terms with Eq. (1c), relative to dP_{gain}/dz. As expected, Fig. 16 shows that an increase in pressure and/or dimension leads to the classical local regime of energy absorption, in which the power losses are exclusively controlled by electron-neutral collisions. Conversely, decreasing NR leads to higher power losses associated to the mechanisms of space-charge sheath maintenance. Numerical tests reveal that the power deposition features depicted in this figure are almost independent of variations in the average electron density.

TABLE I. Typical parameters characterizing the electron heating within resonance region. Results were obtained for the cylindrical structure.

$\bar{n}_e$ (cm^{-3})	p (Torr)	Δ (cm)	E_{hf}/N (V cm^2)	τ_{dc} (s)	τ_{hf} (s)	$\varepsilon_c^{\mathrm{res}}$ (eV)	$\varepsilon_{\mathrm{nc,max}}^{\mathrm{res}}$ (eV)	ΔV_s (V)	ε (eV)
7×10^{11}	0.01	7.9×10^{-5}	5.9×10^{-10}	4.0×10^{-11}	4.8×10^{-12}	36.7	4.5	33.3	8.0
	0.1	4.9×10^{-4}	5.8×10^{-12}	4.0×10^{-10}	3.5×10^{-11}	32.0	2.7	19.4	4.4
	5	7.1×10^{-2}	7.7×10^{-16}	1.2×10^{-6}	4.8×10^{-8}	67.3	2.6	13.3	2.0
10^{12}	0.01	5.7×10^{-5}	8.1×10^{-10}	2.0×10^{-11}	2.5×10^{-12}	35.3	4.5	33.2	7.9
	0.1	3.5×10^{-4}	7.6×10^{-12}	2.1×10^{-10}	1.9×10^{-11}	28.0	2.6	19.3	4.4
	5	4.9×10^{-2}	1.0×10^{-15}	5.8×10^{-7}	2.5×10^{-8}	56.9	2.4	13.5	2.0
3×10^{12}	0.01	2.4×10^{-5}	2.1×10^{-9}	3.1×10^{-12}	4.1×10^{-13}	36.4	4.9	33.0	7.9
	0.1	1.4×10^{-4}	1.8×10^{-11}	2.8×10^{-11}	3.2×10^{-12}	21.3	2.4	19.3	4.4
	5	1.3×10^{-2}	2.5×10^{-15}	5.3×10^{-8}	2.7×10^{-9}	30.9	1.6	13.6	2.0

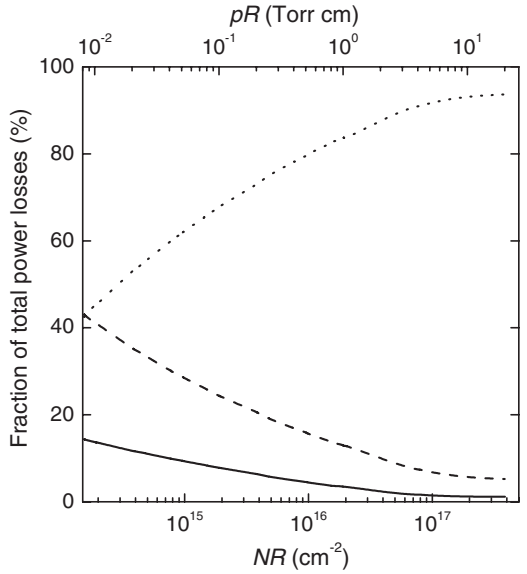

FIG. 16. Fraction of total power losses, as a function of NR (and pR), for the cylindrical structure at $\bar{n}_e = 10^{12}$ cm^{-3}. The different curves correspond to the following power loss channels [see Eq. (1c)]: Convection flow (solid curve); collisional cooling in diffusion against the space-charge field (dashed curve); friction due to elastic and inelastic collisions (dotted curve).

B. Results for the coaxial structure

The present modeling work is complemented by the study of a coaxial structure, in which the plasma surrounds the inner excitation antenna. Essentially, the simulation results for this structure are similar to those presented before for the cylindrical structure. The main different features are the development of two space-charge sheath regions (leading to two electron-plasma resonances), near the dielectric and the outer conductor.

Figure 17 shows the profiles of the reduced electron density $n_e/n_e(r_c)$, at $\bar{n}_e = 10^{12}$ cm^{-3} for $p = 0.03, 0.1, 0.5, 2$ Torr. These profiles feature a maximum value in the vicinity of the critical position and very steep gradients in the sheath regions. Notice that neither the left branch of the density distribution nor the critical position is very much affected by pressure variations, whereas the right branch exhibits the pressure dependence already observed for the cylindrical structure. Figure 18 presents the radial distribution (across the coaxial structure) of E_r, E_z, and H_φ (the latter multiplied by a factor of 10^3), normalized to $E_z(R_{c,\mathrm{in}})$, at $\bar{n}_e = 10^{12}$ cm^{-3} and $p = 100$ mTorr (corresponding to a calculated incident power $P_{\mathrm{inc}} \simeq 1$ kW). The results in this figure confirm the development of a double resonance phenomenon, near each of the plasma boundaries (see the insets within).

C. Similarity curve for the power absorbed by the plasma

The results of the total power absorbed by the plasma, for different discharge structures and for different work conditions, can be correlated by resorting to a universal similarity curve. The concept of similarity curve was first introduced to describe the maintenance of the positive column of dc discharges [106,107]. This curve is obtained by representing the reduced excitation field E/N (or, equivalently, the electron temperature T_e), as a function of the product of the gas density by the discharge radius, NR (or, equivalently, the product of the pressure by the discharge radius, pR). The fact that this representation yields practically a single curve, even for different discharge conditions, means that E/N is an almost unique function of NR, hence independent of the electron density or the populations of the excited states with the neutral gas. Although this result gives only a simple, approximate picture of discharge maintenance [108,109], the fact remains that experimental studies confirm the concept of a

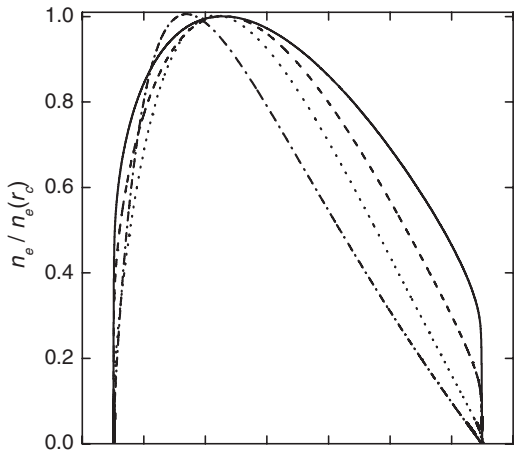

FIG. 17. Radial profiles of the reduced electron density $n_e/n_e(r_c)$, for the coaxial structure at $\bar{n}_e = 10^{12}$ cm^{-3} and the following values of p (in Torr) [corresponding to the following values of $n_e(r_c)$ (in cm^{-3})]: 0.03 [$n_e(r_c) = 1.3 \times 10^{12}$] (solid curves); 0.1 [$1.5 \times 10^{12}$] (dashed curves); 0.5 [$1.8 \times 10^{12}$] (dotted curves); 2 [$2.1 \times 10^{12}$] (dashed-dotted curves).

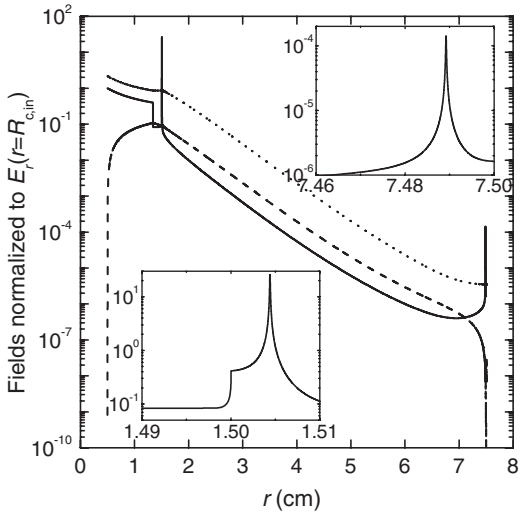

FIG. 18. Radial distribution (across the coaxial structure) of the SW electromagnetic field components, normalized to $E_r(R_{c,\mathrm{in}})$, at $\bar{n}_e = 10^{12}$ cm^{-3} and $p = 100$ mTorr: E_r (solid curve); E_z (dashed curve); $H_\varphi \times 1000$ (dotted curve). The insets are blowups of the E_r profile, over resonance regions.

similarity curve since early measurements of T_e vs pR [106,107]. However, it is known that the evolution of E/N as a function of pR can exhibit some deviations from a universal behavior, due to the presence of stepwise ionization processes [107], the influence of recombination mechanisms [110] (particularly at high pressures or radii), and the effect of gas heating [111,112], especially at high electron densities. Good revisions on the theory of the positive column, presenting information related to the behavior of similarity curves, can be found in Refs. [113–115].

In microwave discharges, the concept of similarity curve was first used in the framework of their homogeneous description [78,116], and was later extended to hf plasmas sustained by nonuniform fields [68,69]. For these discharges, similarity curves are usually associated to the plots of the power required to sustain an electron-ion pair at unit gas density, Θ/N [see Eq. (1c)], as a function of NR. In the present case of a spatially resolved description, we must further account for the radial profiles with the different quantities defining Θ, even if the fractional power loss plotted in Fig. 16 is quasi-independent of $\bar{n}_e$. The solution comes to introduce an average power gained per electron from the SW field, defined as

$$\Theta_{\mathrm{av}} \equiv \frac{\overline{\Theta(r) n_e(r)}}{\overline{n_e(r)}} = \frac{1}{\overline{n_e(r)} \int_{\mathrm{plasma}} 2\pi r dr} \frac{dP_{\mathrm{gain}}}{dz}, \qquad (18)$$

which can be combined with Eq. (14) to deduce the classical law for the axial variation of the electron density, in SW-sustained discharges [39,67]. Moreover, to obtain a similarity curve, the parameter that multiplies the gas density must be replaced by an effective discharge length R_{eff} (associated to the actual size of the plasma), with $R_{\mathrm{eff}}=R$ and $R_{\mathrm{eff}}=R-R_d$ for the one-dimensional description of cylindrical and coaxial structures, respectively.

Figure 19 plots the similarity curve Θ_{av}/N vs NR_{eff}, calculated with the self-consistent model developed here, for radially resolved microwave discharges (with both cylindrical and coaxial configurations), at various pressures, radii, and average electron densities. This plot ensures the alignment, along a single universal curve, of the different operating points obtained for different work conditions and discharge structures. For comparison, this figure also shows the results of the power required to sustain the plasma obtained with the simplified model, which neglects the sheath region. As observed, this model version underestimates the power absorbed by the plasma at low pressure (with respect to the predictions of the complete model), thus confirming the influence of the sheath-resonance region upon discharge maintenance.

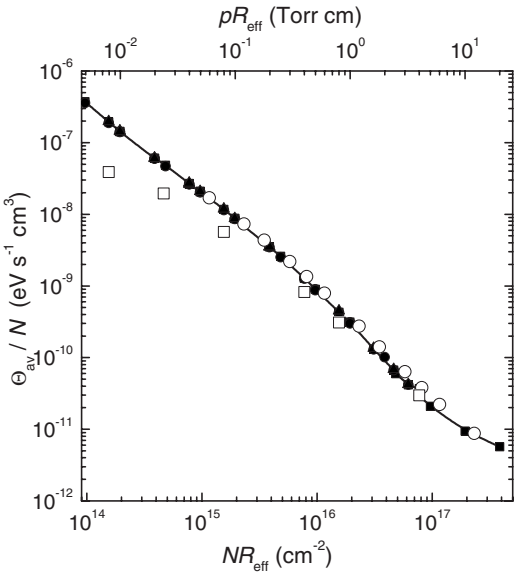

FIG. 19. Similarity curve of Θ_{av}/N vs NR_{eff} (and pR_{eff}), calculated with the complete model developed here, for spatially resolved microwave discharges with cylindrical symmetry. The closed points are from calculations for cylindrical structures, at $p=0.01-5$ Torr; $R=0.5-4$ cm, and the following values of $\bar{n}_e$ (in cm^{-3}): 5×10^{11} (circles); 10^{12} (squares); 5×10^{12} (triangles). The open circles are from calculations for the coaxial structure considered here, at $\bar{n}_e=10^{12}$ cm^{-3} and $p=0.01-2$ Torr. The open squares are from calculations, using a simplified model version that neglects the sheath region, for the cylindrical structure considered here at $\bar{n}_e=10^{12}$ cm^{-3} and $p=0.01-5$ Torr. The solid curve is a fit to all points calculated with the complete model.

VI. SUMMARY AND OUTLOOK

This paper has studied the radial structure of magnetic-free surface-wave (SW) discharges, excited in either a cylindrical or a coaxial structure, by solving a stationary, one-dimensional moment model. The model solves the continuity and the momentum-transfer equations for electrons and positive ions, as well as the electron mean energy transport equations, self-consistently coupled to Poisson's equation for the electrostatic space-charge field and to Maxwell's equations for the TM_{00} electromagnetic fields of a SW propagation mode. The discharge power deposition was described by considering additional terms apart from the classical collisional heating (the power gained by electrons from the SW field), and friction (power lost in electron-neutral collisions). The extra terms account for collisional cooling (power lost by electrons in diffusion against the space-charge field), and power transport due to convection (including a term of drift under the action of the space-charge field, and a collisionless pressure-gradient term). The description of the wave-plasma energy coupling (accounting for the SW collisional dispersion characteristics, with the formation of electron-plasma resonances) used the SW attenuation constant α (obtained either as an eigenvalue to Maxwell's equations or from the electron power balance equation) to check for the physical coherence of model results. A semianalytical approach was used to integrate Maxwell's equations over resonance regions, thus preventing numerical problems associated with the rapid variation of plasma parameters therein. Other features with this SW discharge model were the joint description of sheath-resonance regions and the accounting for the spatial dependence of all electron transport parameters and rate coefficients, by using the local mean energy approximation.

The results obtained with the model developed here were compared to those of a simplified model version, which

adopted the approximations usually considered in the classical description of SW discharges. These approximations disregard the sheath region (assuming quasineutral ambipolar conditions and using Bohm's criterion to define the boundary flux), and ignore the spatial dependence of the different electron parameters (with the exception of the electron mean energy and ionization frequency, for which they adopt the local field approximation). Considerable discrepancies were found between the results of the complete and the simplified model. The latter (i) overestimates the profiles of the electron density, thus preventing the formation of electron-plasma resonances (as the condition $\omega_p \simeq \omega$ is never attained), which ultimately affects the profiles of the electromagnetic SW field components; (ii) underestimates the values of the SW attenuation constant (particularly at low pressures and high electron densities), giving a linear variation of α with p, in contrast with the less monotonic evolution predicted by the complete model; (iii) predicts an axis-to-wall increase in the electron mean energy, in opposition to the flat profiles given by the complete model (which includes nonlocal energy transport phenomena); (iv) underestimates the power absorbed by the plasma at low pressure, which confirms the influence of the sheath-resonance region upon discharge maintenance.

Simulations confirmed that resonance peaks become wider (and simultaneously less intense) for either an increase in pressure or a decrease in the average electron density (hence in the electron density gradient at the nearby boundary). Moreover, for pressures around 10 mTorr and average electron densities above 10^{12} cm^{-3}, resonance peaks were unequivocally found inside the corresponding space-charge sheath. The calculated fractional power lost by electrons, due to the various dissipation channels considered, featured a transition to a local regime of energy absorption (where power losses are exclusively controlled by electron-neutral collisions), as pressure increases. Spatially resolved simulations of microwave discharges (with both cylindrical and coaxial configurations), running at various pressures, radii, and average electron densities, have confirmed that power transfer can be represented by a similarity curve of Θ_{av}/N vs NR_{eff}. The quantity Θ_{av} is an average power gained per electron from the SW field, and its definition accounts for the radial profiles with the different quantities involved in the discharge Joule heating term. The parameter R_{eff} is an effective discharge length, associated to the actual size of the plasma. Simulations showed that the absorption of energy from the SW is strongly dependent on resonance features, particularly at low pressures.

The simulations presented here add a contribution to the study of the influence of electron-plasma resonances on energy absorption in SW discharges, whose combined action with convection phenomenon promotes the nonlocal transport and distribution of energy. The discussion on this issue is far from closed, particularly in what concerns a detailed study of noncollisional electron heating mechanisms in resonance regions, such as transit-time heating and resonance mode conversion. These mechanisms were not accounted for in the model developed here, but we have shown that the contribution (if any) of transit-time heating can only occur for intermediate pressures, around 100 mTorr.

Moreover, our one-dimensional simulations allowed the analysis of nonlocal energy transport (under the influence of electron-plasma resonances) in radial direction, but the overall picture is most likely multidimensional. Recently, directional Langmuir planar probes were used to investigate the presence of high-energy electron fluxes in low-pressure coaxial SW discharges [12,34,35]. The measured probe characteristics exhibited a significant increase in the electronic current over a wide range of probe potentials, with a strong dependence on the radial position and the direction of observation. These anisotropic features, which are probably induced by local plasma resonances, put forward cross-linked radial and axial effects, thus showing that a full description of the boundary phenomena concerned will only be achieved in the framework of a self-consistent two-dimensional model, to be developed still.

ACKNOWLEDGMENTS

The authors thank Dr. P. Leprince for many fruitful discussions about the main features of surface-waves propagation. The authors are also indebted to L. Novo, for some of the simulations presented, and to Dr. J. P. Bizarro, for judicious advice during the reviewing phase of this paper.

[1] M. Moisan, A. Shivarova, and A. W. Trivelpiece, Plasma Phys. **24**, 1331 (1982).
[2] J. Marec, E. Bloyet, M. Chaker, P. Leprince, and P. Nghiem, in *Electric Breakdown and Discharges in Gases. Macroscopic Processes and Discharges*, Vol. 89b of NATO Advanced Study Institute, Series B: Physics, edited by L. H. Luessen and E. E. Kunhardt (Plenum, New York, 1983), p. 347.
[3] M. Moisan and Z. Zakrzewski, in *Radiative Processes in Discharge Plasmas*, Vol. 149 of NATO Advanced Study Institute, Series B: Physics, edited by J. M. Proud and L. H. Luessen (Plenum, New York, 1986), p. 381.
[4] M. Moisan and Z. Zakrzewski, J. Phys. D **24**, 1025 (1991).
[5] *Microwave Excited Plasmas*, edited by M. Moisan and J. Pelletier (Elsevier, Amsterdam, 1992).
[6] *Microwave Discharges: Fundamentals and Applications*, Vol. 302 of NATO Advanced Study Institute, Series B: Physics, edited by C. M. Ferreira and M. Moisan (Plenum, New York, 1993).
[7] Z. Zakrzewski and M. Moisan, Plasma Sources Sci. Technol. **4**, 379 (1995).
[8] I. Zhelyazkov and V. Atanassov, Phys. Rep. **255**, 79 (1995).
[9] H. Sugai, I. Ghanashev, and M. Nagatsu, Plasma Sources Sci. Technol. **7**, 192 (1998).
[10] L. L. Alves and G. Gousset, in *Microwave Discharges: Fundamental and Applications*, edited by A. Ohl (INP Greifswald, Germany, 2003), p. 90.

[11] L. L. Alves, Eur. Phys. J.: Appl. Phys. **26**, 195 (2004).
[12] S. Letout, L. L. Alves, C. Boisse-Laporte, and P. Leprince, J. Optoelectron. Adv. Mater. **5**, 7 (2005).
[13] L. L. Alves, S. Letout, C. Boisse-Laporte, and P. Leprince, in *Microwave Discharges: Fundamental and Applications*, edited by Yu. A. Lebedev (Yanus-K, Moscow, Russia, 2006), p. 177.
[14] A. Metze, D. W. Ernie, and H. J. Oskam, Phys. Rev. A **39**, 4117 (1989).
[15] J. H. Ingold, Phys. Rev. E **56**, 5932 (1997).
[16] L. L. Alves, G. Gousset, and S. Vallée, IEEE Trans. Plasma Sci. **31**, 572 (2003).
[17] I. Ghanashev, H. Sugai, S. Morita, and N. Toyoda, Plasma Sources Sci. Technol. **8**, 363 (1999).
[18] K. N. Stepanov, Sov. Phys. Tech. Phys. **10**, 773 (1970).
[19] A. I. Akhiezer and A. Bakai, Sov. Phys. Dokl. **16**, 1065 (1972).
[20] M. Zethoff and U. Kortshagen, J. Phys. D **25**, 1574 (1992).
[21] Yu. M. Aliev, V. Yu. Bychenkov, A. V. Maximov, and H. Schlüter, Plasma Sources Sci. Technol. **1**, 126 (1992).
[22] Yu. M. Aliev, A. V. Maximov, U. Kortshagen, H. Schlüter, and A. Shivarova, Phys. Rev. E **51**, 6091 (1995).
[23] S. Grosse, M. Georgieva-Grosse, I. Ghanashev, and M. Schlüter, J. Electromagn. Waves Appl. **11**, 609 (1997).
[24] Yu. M. Aliev, H. Schlüter, and A. Shivarova, in *Guided-Wave Produced Plasmas*, Vol. 24 of Springer Series on Atoms and Plasmas, edited by G. Ecker (Springer-Verlag, New York, 2000), pp. 33, 79.
[25] A. Durandet, Y. Arnal, J. Margot-Chaker, and M. Moisan, J. Phys. D **22**, 1288 (1989).
[26] H. Sugai, T. H. Ahn, I. Ghanashev, M. Goto, M. Nagatsu, K. Nakamura, K. Suzuki, and H. Toyoda, Plasma Phys. Controlled Fusion **39**, A445 (1997).
[27] E. Räuchle, J. Phys. IV **8**, Pr7-99 (1998).
[28] H. Sugai, I. Ghanashev, and K. Mizuno, Appl. Phys. Lett. **77**, 3523 (2000).
[29] T. J. Wu, W. J. Guan, C. M. Tsai, M. Y. Yeh, and C. S. Kou, Phys. Plasmas **8**, 3195 (2001).
[30] M. Nagatsu, T. Niwa, and H. Sugai, Appl. Phys. Lett. **81**, 1966 (2002).
[31] T. Terebessy, M. Kando, and J. Kudela, Appl. Phys. Lett. **77**, 2825 (2000).
[32] J. Kudela, T. Terebessy, and M. Kando, Appl. Phys. Lett. **76**, 1249 (2000).
[33] T. Terebessy, M. Širý, M. Kando, J. Kudela, and D. Korzec, Appl. Phys. Lett. **82**, 694 (2003).
[34] S. Letout, C. Boisse-Laporte, and L. L. Alves, Appl. Phys. Lett. **89**, 241502 (2006).
[35] S. Letout, P. Leprince, L. Teulé-Gay, L. L. Alves, and C. Boisse-Laporte, in *Microwave Discharges: Fundamental and Applications*, edited by Yu. A. Lebedev (Yanus-K, Moscow, Russia, 2006), p. 51.
[36] I. P. Ganachev and H. Sugai, Plasma Sources Sci. Technol. **11**, A178 (2002).
[37] R. Darchicourt, S. Pasquiers, C. Boisse-Laporte, P. Leprince, and J. Marec, J. Phys. D **21**, 293 (1988).
[38] C. M. Ferreira, J. Phys. D **22**, 705 (1989).
[39] V. M. M. Glaude, M. Moisan, R. Pantel, P. Leprince, and J. Marec, J. Appl. Phys. **51**, 5693 (1980).
[40] E. Mateev, I. Zhelyazkov, and V. Atanassov, J. Appl. Phys. **54**, 3049 (1983).
[41] Z. Zakrzewski, J. Phys. D **16**, 171 (1983).
[42] Yu. M. Aliev, A. G. Boev, and A. P. Shivarova, J. Phys. D **17**, 2233 (1984).
[43] I. Zhelyazkov, E. Benova, and V. Atanassov, J. Appl. Phys. **59**, 1466 (1986).
[44] C. Boisse-Laporte, A. Granier, E. Dervisec, P. Leprince, and J. Marec, J. Phys. D **20**, 197 (1987).
[45] A. Granier, C. Boisse-Laporte, P. Leprince, J. Marec, and P. Nghiem, J. Phys. D **20**, 204 (1987).
[46] C. Boisse-Laporte, A. Granier, E. Bloyet, P. Leprince, and J. Marec, J. Appl. Phys. **61**, 1740 (1987).
[47] I. Zhelyazkov and E. Benova, J. Appl. Phys. **66**, 1641 (1989).
[48] E. Benova and I. Zhelyazkov, Phys. Scr. **43**, 68 (1991).
[49] Yu. M. Aliev, K. M. Ivanova, M. Moisan, and A. Shivarova, Plasma Sources Sci. Technol. **2**, 145 (1993).
[50] Yu. M. Aliev, I. Ghanashev, H. Schlüter, A. Shivarova, and M. Zethoff, Plasma Sources Sci. Technol. **3**, 216 (1994).
[51] U. Kortshagen, H. Schlüter, and A. Shivarova, J. Phys. D **24**, 1571 (1991).
[52] U. Kortshagen and H. Schlüter, J. Phys. D **25**, 644 (1992).
[53] U. Kortshagen, J. Phys. D **26**, 1230 (1993).
[54] C. M. Ferreira and J. Loureiro, J. Phys. D **16**, 2471 (1983).
[55] C. M. Ferreira and J. Loureiro, J. Phys. D **17**, 1175 (1984).
[56] C. M. Ferreira and J. Loureiro, J. Phys. D **22**, 76 (1989).
[57] L. L. Alves, G. Gousset, and C. M. Ferreira, J. Phys. D **25**, 1713 (1992).
[58] P. A. Sá, J. Loureiro, and C. M. Ferreira, J. Phys. D **27**, 1171 (1994).
[59] G. M. Petrov, J. P. Matte, I. Pérès, J. Margot, T. Sadi, J. Hubert, K. C. Tran, L. L. Alves, J. Loureiro, C. M. Ferreira, V. Guerra, and G. Gousset, Plasma Chem. Plasma Process. **20**, 183 (2000).
[60] E. Benova, Ts. Petrova, A. Blagoev, and I. Zhelyazkov, J. Appl. Phys. **84**, 147 (1998).
[61] Ts. Petrova, E. Benova, G. Petrov, and I. Zhelyazkov, Phys. Rev. E **60**, 875 (1999).
[62] E. Tatarova, F. M. Dias, C. M. Ferreira, V. Guerra, J. Loureiro, E. Stoykova, I. Ghanashev, and I. Zhelyazkov, J. Phys. D **30**, 2663 (1997).
[63] E. Tatarova, F. M. Dias, C. M. Ferreira, and A. Ricard, J. Appl. Phys. **85**, 49 (1999).
[64] B. Gordiets, M. Pinheiro, E. Tatarova, F. M. Dias, C. M. Ferreira, and A. Ricard, Plasma Sources Sci. Technol. **9**, 295 (2000).
[65] V. Guerra, E. Tatarova, F. M. Dias, and C. M. Ferreira, J. Appl. Phys. **91**, 2648 (2002).
[66] C. M. Ferreira, J. Phys. D **14**, 1811 (1981).
[67] C. M. Ferreira, J. Phys. D **16**, 1673 (1983).
[68] C. M. Ferreira and M. Moisan, Phys. Scr. **38**, 382 (1988).
[69] A. B. Sá, C. M. Ferreira, S. Pasquiers, C. Boisse-Laporte, P. Leprince, and J. Marec, J. Appl. Phys. **70**, 4147 (1991).
[70] X. L. Zhang, F. M. Dias, and C. M. Ferreira, Plasma Sources Sci. Technol. **6**, 29 (1997).
[71] K. U. Riemann, J. Phys. D **24**, 493 (1991).
[72] I. Pérès, M. Fortin, and J. Margot, Phys. Plasmas **3**, 1754 (1996).
[73] I. Pérès and J. Margot, Plasma Sources Sci. Technol. **5**, 653 (1996).
[74] P. A. Sá, J. Loureiro, and C. M. Ferreira, J. Phys. D **25**, 960 (1992).

[75] W. Petasch, E. Räuchle, H. Muegge, and K. Muegge, Surf. Coat. Technol. **93**, 112 (1997).
[76] M. Kaiser, K. M. Baumgärtner, A. Schulz, M. Walker, and E. Räuchle, Surf. Coat. Technol. **116**, 552 (1999).
[77] R. F. Whitmer and G. F. Herrmann, Phys. Fluids **9**, 768 (1966).
[78] C. M. Ferreira, in *Nonequilibrium Processes in Partially Ionized Gases*, edited by M. Capitelli and J. N. Bardsley (Plenum, New York, 1990), p. 187.
[79] G. Gozadinos, M. M. Turner, and D. Vender, Phys. Rev. Lett. **87**, 135004 (2001).
[80] M. M. Turner, Phys. Rev. Lett. **71**, 1844 (1993).
[81] R. L. Stenzel, A. Y. Wong, and H. C. Kim, Phys. Rev. Lett. **32**, 654 (1974).
[82] L. L. Alves, G. Gousset, and C. M. Ferreira, Phys. Rev. E **55**, 890 (1997).
[83] M. Surendra and M. Dalvie, Phys. Rev. E **48**, 3914 (1993).
[84] J. H. Ingold, in *Electron Kinetics and Applications of Glow Discharges*, Vol. 369 of NATO Advanced Study Institute, Series B: Physics, edited by U. Kortshagen and L. D. Tsendin (Plenum, New York, 1998), p. 101.
[85] P. M. Meijer, W. J. Goedheer, and J. D. P. Passchier, Phys. Rev. A **45**, 1098 (1992).
[86] M. Meyyappan and T. R. Govindan, J. Appl. Phys. **74**, 2250 (1993).
[87] G. J. Nienhuis, W. J. Goedheer, E. A. G. Hamers, W. G. J. H. M. van Sark, and J. Bezemer, J. Appl. Phys. **82**, 2060 (1997).
[88] E. Kawamura and J. H. Ingold, J. Phys. D **34**, 3150 (2001).
[89] A. Salabas, G. Gousset, and L. L. Alves, Plasma Sources Sci. Technol. **11**, 448 (2002).
[90] I. B. Bernstein and T. Hosltein, Phys. Rev. **94**, 1475 (1954).
[91] L. D. Tsendin, Zh. Eksp. Teor. Fiz. **66**, 1638 (1974) [Sov. Phys. JETP **39**, 805 (1974)].
[92] L. D. Tsendin and Y. B. Golubovskii, Zh. Tekh. Fiz. **47**, 1839 (1977) [Sov. Phys. Tech. Phys. **22**, 1066 (1977)].
[93] L. D. Tsendin, Zh. Tekh. Fiz. **48**, 1569 (1978) [Sov. Phys. Tech. Phys. **23**, 890 (1978)].
[94] U. Kortshagen, J. Phys. D **26**, 1691 (1993).
[95] L. D. Tsendin, Plasma Sources Sci. Technol. **4**, 200 (1995).
[96] U. Kortshagen, Plasma Sources Sci. Technol. **4**, 172 (1995).
[97] U. Kortshagen, C. Busch, and L. D. Tsendin, Plasma Sources Sci. Technol. **5**, 1 (1996).
[98] U. Kortshagen, G. J. Parker, and J. E Lawler, Phys. Rev. E **54**, 6746 (1996).
[99] S. Pfau, J. Rohmann, D. Uhrlandt, and R. Winkler, Contrib. Plasma Phys. **36**, 449 (1996).
[100] V. E. Golant, A. P. Zhilinsky, and I. E. Sakharov, in *Fundamentals of Plasma Physics*, edited by S. C. Brown (Wiley, New York, 1980).
[101] H. B. Valentini, E. Glauche, and D. Wolff, Plasma Sources Sci. Technol. **4**, 353 (1995).
[102] V. L. Ginzburg, *Propagation of Electromagnetic Waves in Plasma* (North-Holland, Amsterdam, 1960), p. 319.
[103] D. L. Scharfetter and H-K. Gummel, IEEE Trans. Electron Devices **16**, 64 (1969).
[104] A. Yanguas, J. Cotrino, and L. L. Alves, J. Phys. D **38**, 1588 (2005).
[105] D. M. Manos and D. L. Flamm, *Plasma Etching—An Introduction* (Academic, New York, 1989).
[106] S. C. Brown, *Basic Data of Plasma Physics* (MIT Press, Cambridge, MA, 1966), and references therein.
[107] A. von Engel, *Ionized Gases* (Clarendon, Oxford, 1965), and references therein.
[108] B. E. Cherrington, *Gaseous Electronics and Gas Lasers* (Pergamon, Oxford, 1979), and references therein.
[109] Y. M. Kagan and R. I. Lyagushchenko, Sov. Phys. Tech. Phys. **7**, 134 (1962).
[110] L. J. Denes and J. J. Lowke, Appl. Phys. Lett. **23**, 130 (1973).
[111] G. Ecker and O. Zoller, Phys. Fluids **7**, 1996 (1964).
[112] I. M. Cohen and A. M. Whitman, Phys. Fluids **16**, 307 (1973).
[113] G. Ecker, Proc. Phys. Soc. London, Sect. B **67**, 485 (1954).
[114] R. A. Gerber and J. B. Gerardo, Phys. Rev. A **7**, 781 (1973).
[115] J. H. Ingold, Phys. Fluids **15**, 75 (1975).
[116] C. M. Ferreira, L. L. Alves, M. Pinheiro, and A. B. Sá, IEEE Trans. Plasma Sci. **19**, 229 (1991).